

DESIGN OPTIMIZATION OF FOLDING SOLAR POWERED AUTONOMOUS  
UNDERWATER VEHICLES USING ORIGAMI STRUCTURE

A Thesis

by

DOE YOUNG HUR

Submitted to the Office of Graduate and Professional Studies of  
Texas A&M University  
in partial fulfillment of the requirements for the degree of

MASTER OF SCIENCE

Chair of Committee,	Richard J. Malak
Committee Members,	Darren J. Hartl
	Douglas Allaire
Head of Department,	Andreas A. Polycarpou

August 2017

Major Subject: Mechanical Engineering

Copyright 2017 Doe Young Hur

## ABSTRACT

Origami, as an application for morphing structure engineering, which has been studied for a long time, has recently made remarkable progress in terms of technology. The most distinctive feature of this technology is the presence of two types, flat mode and folded mode. The origami algorithm enables the conversion of these two modes based on the mathematical formulations. Completion of this algorithm now means that origami is part of the design process and can be applied to applications.

This thesis demonstrates a design process for origami-inspired morphing structures that transform between a flat configuration and a folded convex shape. There are many obstacles in the development of the design process. In particular, consideration should be given to the surface difference of the flat configuration and the folded convex mode. In this thesis, I introduce the design process which takes into consideration the origami structure design deeply.

To demonstrate this process, I have selected an application which is emerging and interesting, that is, unmanned vehicles. Especially, the design of Autonomous Underwater Vehicles (AUVs) is a difficult challenge since it requires the consideration of various aspects such as mission range, controllability, energy source, and carrying capacity. The Predictive Parameterized Pareto Genetic Algorithm (P3GA) is selected as the optimization method to determine a parameterized Pareto frontier of design options with desired characteristics for a variety of missions for the AUV.

## ACKNOWLEDGEMENTS

I would like to thank my committee chair, Dr. Richard Malak and committee member Dr. Darren Hartl for full support and guidance in minute detail. Committee member Dr. Douglas Allaire, for the support throughout the course of this research.

## CONTRIBUTORS AND FUNDING SOURCES

This work is supported by the National Science Foundation and the Air Force Office of Scientific Research under grant EFRI-1240483. Any opinions, findings, conclusions or recommendations are those of the authors and do not necessarily reflect the views of the U.S. Air Force. The authors would like to acknowledge Dr. Douglas Allaire for providing the main idea for the study presented in this work. Computational fluid analysis was performed using a research license granted by ANSYS. The optimization studies were conducted using Matlab, courtesy of Mathworks.

## NOMENCLATURE

$H1$	Height of AUV (m)
$L1$	Length of front region (m)
$L2$	Length of rear region (m)
$KR1, KR2$	Input variables of shape function
$d$	Characteristic length of the mesh faces (m)
$w$	Characteristic length of the tucked regions in the origami design (m)
$C$	Length of AUV for shape function (m)
$Z$	Height of AUV for shape function (m)
$C_D$	Drag coefficient
$C_M$	Moment coefficient
$Area$	Available area for solar panel (m <sup>2</sup> )
$Volume$	Available volume inside the body (m <sup>3</sup> )
$\eta_e$	Efficiency of electrical speed controller
$\eta_P$	Efficiency of propeller
$\eta_M$	Efficiency of motor
$E_c$	Collected energy
$Drag$	Drag force

## TABLE OF CONTENTS

ABSTRACT .....	ii
ACKNOWLEDGEMENTS .....	iii
CONTRIBUTORS AND FUNDING SOURCES.....	iv
NOMENCLATURE.....	v
TABLE OF CONTENTS .....	vi
LIST OF FIGURES.....	viii
LIST OF TABLES .....	x
1. INTRODUCTION.....	1
2. ENGINEERING DESIGN PROBLEMS .....	6
2.1. Origami Structure.....	6
2.2. Solar Powered Autonomous Underwater Vehicle.....	8
2.3. Overall Design Process.....	10
3. ANALYSIS AND OPTIMIZATION TOOLS.....	15
3.1. Three-dimensional Modeling based on Shape Function.....	15
3.2. Origami Modeling.....	18
3.3. Computational Fluid Analysis.....	21
3.4. Available Solar Area Calculation.....	23
3.5. Available Inner Volume Calculation.....	24
3.6. Mission Range Calculation.....	27
3.7. Parametric Optimization using P3GA.....	28

4. RESULTS.....	31
4.1. Design of Experiment.....	31
4.2. Validation of Models.....	34
4.3. Physical Characteristics.....	39
4.4. Pareto Front.....	47
5. CONCLUSIONS.....	51
REFERENCES.....	52

## LIST OF FIGURES

Figure 1. Trade-off between Folded Convex and Flat Configuration.....	3
Figure 2. Planar Configuration of Designed Origami Sheet that Maximizes Projected Area of Solar Panels (Top), Goal Configuration Obtained after Folding (Bottom).....	7
Figure 3. Concept Design of Solar Powered AUV, Adapted from [36] .....	9
Figure 4. Overall Design Process .....	12
Figure 5. Flowchart of Analysis Approach .....	12
Figure 6. Side View and Top View of The AUV Shape and Brief Description of Dimension Parameters .....	16
Figure 7. AUV Model with H1=1.27 m, L1=1.05 m, L2=3.3 m (LEFT) and H1=0.72 m, L1=0.85 m, L2=3.74 m (Right) .....	17
Figure 8. An illustration of an existing advanced front mesh generation concept in two dimensions. The dotted line indicates the current front. The new triangle is created one at a time by joining the two leading edges to the newly created point or existing lead .....	19
Figure 9. Three-Dimensional Model Before Meshing (Top) and After Meshing (Bottom).....	20
Figure 10. Example Of Triangular Solar Panel, Adapted from [52].....	23
Figure 11. Edge-tucking molecule is represented in terms of two parameters: $w$ and $\theta$ , Adapted from [53] .....	24
Figure 12. (a) Vertex-tucking molecule surrounded by polygons and edge-tucking molecules. (b) Vertex-tucking molecule on the boundary, Adapted from [53].....	25
Figure 13. Comparison of Same Model With Different $w$ Value. Same model with $w=0.2$ (Top, Available Inner Volume = $2.497 \text{ m}^3$ ) and $w=0.6$ (Bottom, Available Inner Volume = $1.165 \text{ m}^3$ ) .....	27
Figure 14. Flow chart of the P3GA, Adapted from [15] .....	29
Figure 15. An illustration of predicted dominance, Adapted from [60] .....	30
Figure 16. Examples of Latin Hypercube Designs, Adapted from [74] .....	32

Figure 17. Distribution of Experimental Points (First Generation), Design of Experiment (TOP), Optimization (BOTTOM).....	33
Figure 18. Experimental Points (25th Generation), H1 vs CD .....	33
Figure 19. Base Model – 1/10 Scale Typhoon Type Submarine .....	34
Figure 20. Manuevering Case Validation Result .....	35
Figure 21. Two Types of Tail Wings for Validation. A-Type (Top) And B-Type (Bottom).....	38
Figure 22. Results of Sensitivity Analysis. H1 vs CD (Top) and d vs CD (Bottom).....	39
Figure 23. Projected Scatter Plot of All Populations: H1 vs. CD (Top) and d Vs. CD (Bottom).....	41
Figure 24. Projected Scatter Plot of All Populations: H1 vs. Drag Force.....	42
Figure 25. Projected Scatter Plot of All Populations w vs. Area .....	42
Figure 26. Projected Scatter Plot of All Populations d vs. Area .....	43
Figure 27. Results of H1 vs. CM grom Sensitivity Analysis (Top) and Projected Scatter Plot (Bottom) .....	43
Figure 28. Projected Scatter Plot of all Populations H1 vs. Inner Volume (Top) and H1 vs Range (Bottom).....	45
Figure 29. Projected Scatter Plot for Range vs Inner Volume of all Populations (TOP) and Non-dominated Populations (BOTTOM).....	46
Figure 30. Three-Dimensional Scatter Plot of all Populations for Design of Experiment.....	47
Figure 31. Three-Dimensional Pareto Frontiers for Design of Experiment.....	48
Figure 32. Three Dimensional Pareto Frontiers via Interpolated Mesh for Optimization .....	49
Figure 33. Three Dimensional Scatter Plot of each Unknown Parameter (H1) for Optimization .....	49

## LIST OF TABLES

Table 1. Drag Coefficient of a Sphere relative to Reynolds number [75] .....	36
Table 2. Validation Results for Origami Piece Size.....	36

## 1. INTRODUCTION

Origami allows for the transformation of initially 2-dimensional sheets to 3-dimensional shapes through folding. Origami engineering is currently applied to an industrial field such as satellites [1]. Although origami-inspired design promise in some situations, it is not currently a widely-used technique in the design of engineered structures and systems. There are two main reasons for this. First, the origami has not been applied to precision machine industries. Second, there is still lack of the technology to properly control the origami-inspired structures for industrial applications.

To properly utilize origami technology, it is necessary to develop an appropriate design process based on an understanding of origami. Unlike the analysis of general rigid structures, the characteristics of origami as a morphing structure must be carefully considered to derive its merits. There are a number of additional things to consider such as total surface area change due difference between the flat configuration and folded convex, and dividing the smooth surface into flat pieces. Therefore, this thesis introduces a design process that can take advantage of the original advantage of origami.

In this thesis, I have applied origami-inspired structures to Solar Powered Autonomous Underwater Vehicle (SAUV) for demonstration. Design of rigid origami, where the planar facets of the sheet are rigid, is an active area of study [2, 3, 4, 5, 6, 7]. Contributions in this area have enabled novel methodologies for the design of deployable structures and morphing architectural forms [2, 8, 9, 10, 11, 12].

The biggest advantage of the designed origami structure is that it is able to transform both the three-dimensional shape and the flat surface repeatedly. In this thesis, I have applied the origami-inspired design to the AUV field.

AUVs have become an application that is widely used in military, oceanographic, and environmental study. Recent AUV development efforts have focused on range and endurance for long-term operation. This enables long-term data collection [13, 14]. Four key characteristics are desired for AUVs: hydrodynamic efficiency, mobility, volume capacity and energy capacity. Among them, energy capacity is the most important. The AUV is able to conduct measurements at remote locations of the ocean [15]. A crucial limiting factor for such vehicles is the limited distance that the AUV can travel with its available energy. This is due to the lack of an inexpensive and effective energy source. Aside from nuclear sources of energy, a potential solution to this challenge is to harvest energy from the environment. An accessible source of energy is solar radiation [16].

In another aspect, some recent works have also considered the problem of finding the optimum hull form for AUVs to minimize drag. These include the works of Lutz and Wagner [17], Bertram and Alvarez [18], and Alvarez and coworkers [19]. Small reductions in hydrodynamic drag can result in substantial savings in thrust requirements and significant improvement in achieving higher vehicle cruising speeds [20, 21]. As you can see in the picture below, you can easily compare two extreme cases. Since the folded SAUV is advantageous in terms of hydrodynamics, the resistance in water is relatively small and the influence of algae is less. However, even if it floats on the

surface of the water, it is not easy to charge because the area exposed to the sun is small. Conversely, in the case of the flat type, it is possible to secure a large amount of chargeable area, but it is difficult to protect the internal equipment and has a hydrodynamic disadvantageous form. Therefore, as shown in Fig.1, origami was applied to the design of SAUV which can take advantage of these two modes.

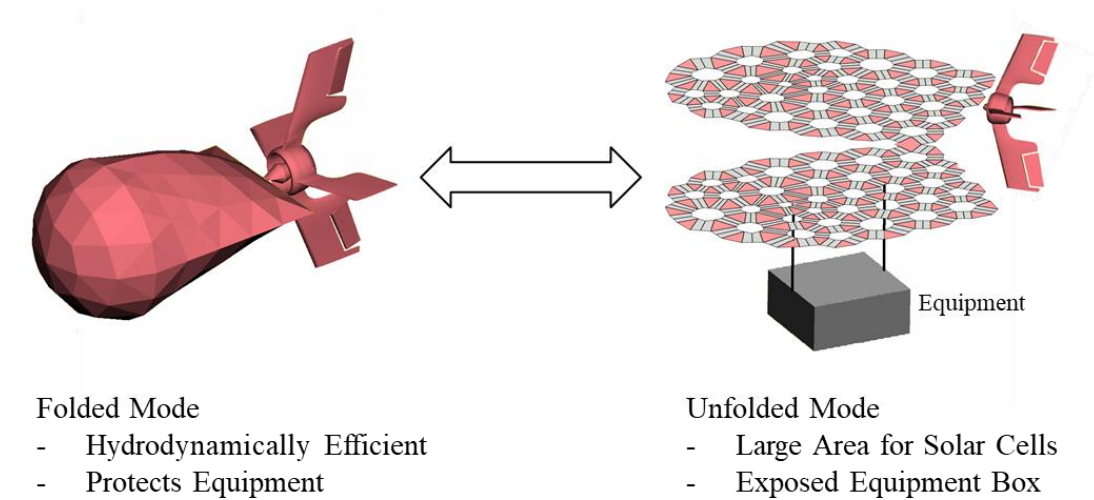


**Figure 1. Trade-off between Folded Convex and Flat Configuration**

There are many obstacles in the development of the design process. In particular, consideration should be given to the surface difference of the flat configuration and the folded convex mode. In this thesis, I introduce the design process which takes into consideration the origami structure design deeply.

More work still needs to be done in terms of optimizing the hull form design to minimize drag or increase propulsion efficiency [22, 23]. In this thesis, the overall shape of a novel process, which is explained in sec 2.3 in detail, for solar-powered AUV is designed.

Since new advances in origami design allow for the realization of three-dimensional goal shapes by folding initially planar sheets, the key step in the design process of an application is to determine the goal shape. A convenient way to describe a three-dimensional surface is through combinations of surface functions such as Non-Uniform Rational B-Splines (NURBS) [12, 13, 14, 24, 25, 26]. Using NURBS, a complex surface can be mathematized through a finite set of variables. For industrial applications where performance is dependent on shape, the method is efficient to seek for an optimum design. Prior to this, however, boundary curves were required to define the NURBS surface, which used an improved shape function for the vehicle [27], is parameterized using a low number of variables allowing for efficient optimization.

An origami design method [28, 29, 30, 31] is used to determine a planar sheet that can be folded towards the AUV shape. As such, origami design allows for the folding/unfolding of the structure between the AUV shape (to store materials and navigate underwater) and the planar shape (to maximize the projected area of the AUV solar panels and to charge the power supplies). The employed origami modeling and design methods consider smooth folds [28, 29, 30], in contrast to creased folds conventionally assumed in the literature. Therefore, the folds considered here can be integrated with active material actuators (since their deformation requires smooth bending [30]).

Furthermore, I explore how these performance characteristics (hydrodynamic efficiency, mobility, volume capacity, and energy capacity) are affected by sizing constraints using parametric optimization [32, 33, 34]. Engineers routinely perform

parameter studies to investigate how a system responds under a range of assumptions. Parametric optimization is an extension that asks how the optimal design changes over the range of parameters. The result is a description of optimal solutions as a function of parameter. In this thesis, I use parametric optimization to explore what ranges of hydrodynamic efficiency, mobility, and energy capacity are achievable as a function of the AUV size. The results give insight into the capabilities and limitations of the solar-powered AUV concept. A previously developed algorithm, predictive parametrized Pareto genetic algorithm (P3GA) [31], is used to solve the search problem.

## 2. ENGINEERING DESIGN PROBLEMS

### 2.1. Origami Structure

The origami design method previously developed by the authors Peraza Hernandez and Hartl [28, 31] is utilized. It provides the geometry of a single planar sheet with a pattern of smooth folds (see Fig. 2) that can morph towards the original input mesh of the AUV. As shown in the literature [30], there are several critical characteristics due to the folding of the origami.

The most important feature of origami-inspired design is the folded convex state. Generally, I can create an origami model that maintains the shape of the initial three-dimensional input model. The novel origami-based design of the AUV proposed here allows the folding and unfolding of the structure between the AUV shape optimized for hydrodynamic efficiency (to navigate underwater and store materials) and the planar shape (to maximizes the projected area of the AUV solar panels to charge the power supplies). The employed origami modeling and design methods consider smooth folds [28, 29, 30] as opposed to creased folds typically assumed in the literature. Therefore, the folds considered here may have integrated active material actuators (since their deformation requires smooth bending [30]). The effect of folding on SAUV can be classified into three types. The volume loss due to the tucked surface of the folded convex, the change in surface area resulting from exposure of the surface in flat configuration, and the change in drag due to sharp edge formation on the smooth surface. The loss of volume is to be treated again at sec 3.5 and surface edge formation at sec 3.1.

Exposed surface area of flat mode is also shown in Fig.1. Unlike the orange colored region, which always exposed in both modes, the gray colored tucked surface and the black colored bended surface are not exposed in folded convex. This difference makes it possible to obtain more exposed areas than conventional single-mode SAUV. Because of the above features, the design process introduced in this thesis should consider two modes at once. In this thesis, we set the objective based on the target performance in each mode and monitor both modes. To improve the performance of AUV mentioned above, we focused on performance such as Available Area, Available Inner Volume, and Drag Force.

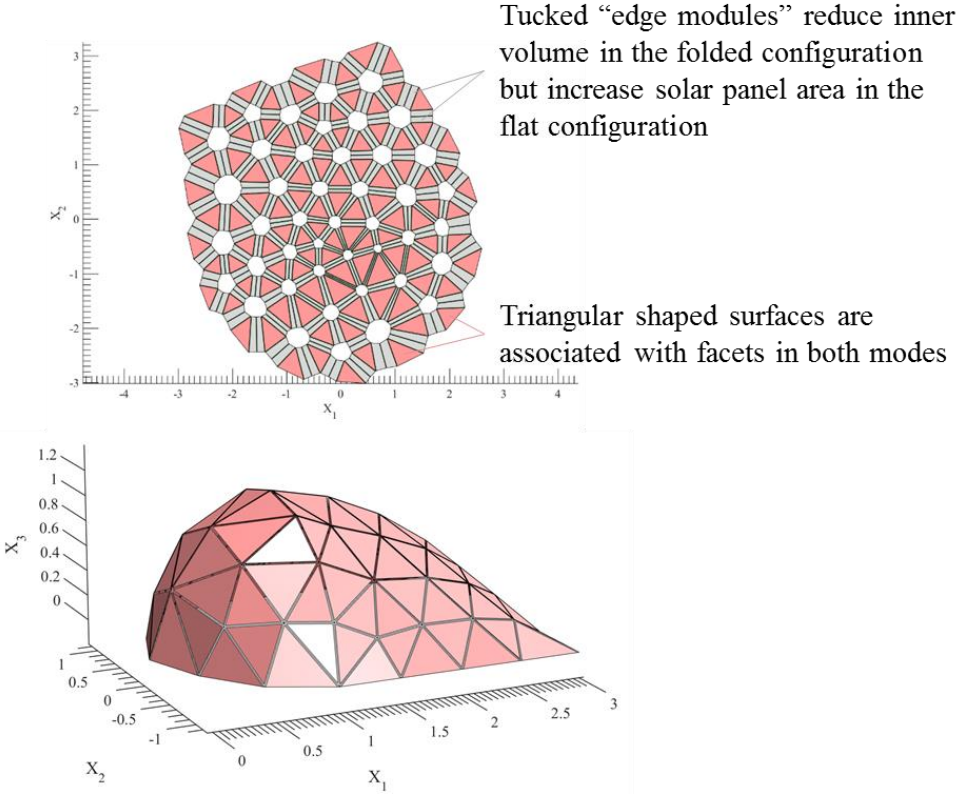


**Figure 2. Planar Configuration of Designed Origami Sheet that Maximizes Projected Area of Solar Panels (Top), Goal Configuration Obtained after Folding (Bottom)**

## 2.2. Solar Powered Autonomous Underwater Vehicle

It has long been considered that AUVs could provide an effective solution for surveillance, environmental monitoring and data portal (to sub-sea instruments) requirements. However, limitations in their battery life have limited the usefulness of AUVs in such applications. Rechargeable solar batteries have been proposed to enhance the application of AUV platforms where long-term or ongoing deployment is required [35]. On the other hands, the importance of oceanographic monitoring has gained importance as the range of human activities has expanded to the ocean. Current amount of data gathered from ocean is not enough to fulfill the requirement to understand chemical, biological and physical characteristics. For example, physical and biological coupling, biogeochemical processes and cycles both natural and human induced, fisheries, and ecosystem modeling need more data to analyze more precisely. However, current data gathering system does not have enough ability to provide enormous size of the data continuously.

To resolve this issue, a Solar-powered Autonomous Vehicle (SAUV) was introduced by Blidberg, et al. As shown in Fig.3 [36], the SAUV utilized the solar energy as an energy source for autonomous data gathering platforms. The model they introduced has several assumptions. They considered the insolation to be 4.0 kWhr/m<sup>2</sup>/day (in the southern US), a 10% of conversion efficiency and the PV array of 1.8m<sup>2</sup>. With these assumptions and the model, they expected 42 km transit at a velocity of 3.5km/hr. [36].

Yet, the design of a SAUVs involves several more competing objectives, it is a good case-study for the adaptation of origami principles and the performance of multi-objective design optimization.

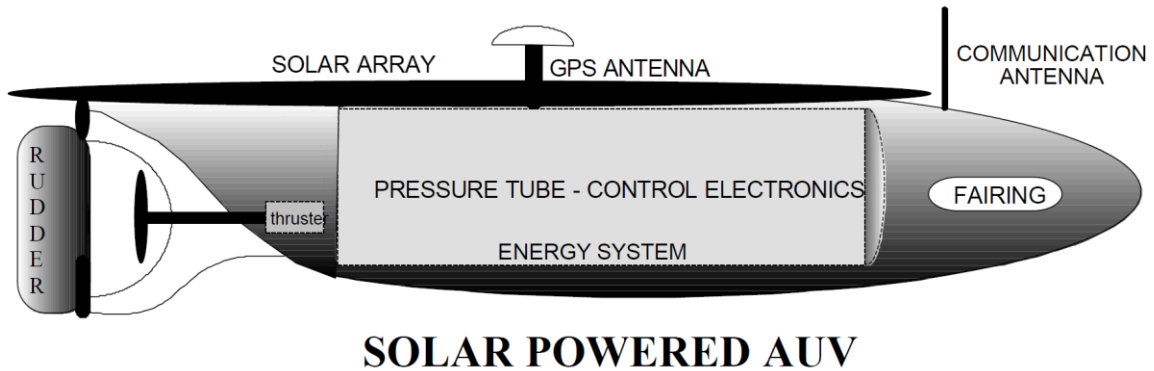


**Figure 3. Concept Design of Solar Powered AUV, Adapted from [36]**

However, this type of AUV is limited by the change of shape due to the solar panel, which limits the drag reduction and controllability. If the shape of an array with a solar cell can be modified, it is very helpful to increase efficiency and mobility. To improve this, I decided to use the origami folding technique. There are two critical characteristics that I can improve through origami. I can expand exposed surface through flat configuration mode and reduce drag through the streamlined form folded convex.

### 2.3. Overall Design Process

Numerous coupling methods have been attempted to perform modeling, analysis, and computation in different fields. One of the biggest obstacles in this process was to synchronize data in different formats. As different logics or computer languages are used, various methods have been discussed to convert the interpreted signal and output data format of each field. For example, C is based on ANSYS Fluent and supercomputing systems, and Rhinoceros is based on C ++. Origami code and P3GA are also compiled by Matlab which is based on C ++. To integrate these languages, I basically used Matlab's batch file processing method, and bundled it into one process using python scripting, which is commonly used for many programs. In addition, the output raw data of each analysis was used in the xls format provided by Microsoft Excel in consideration of the post-processing usability. In addition, three-dimensional model data was used for the igs, inp, and msh formats.

Overall process is shown in Fig.4. It starts with the selection of initial data points using Latin Hypercube Design. For more information on Latin Hypercube Design, see Sec. 4.1. In order to analyze the effectiveness of this process, initial data points were randomly selected in Optimization # 1, and Latin Hypercube Design was applied to Optimization # 2. The analysis process is divided into CFD and origami analysis. The effort in the analysis procedure entails Computational Fluid Dynamics (CFD) analysis. Using ANSYS Fluent, which is fast and accurate, the drag coefficient ( $C_D$ ) and moment coefficient ( $C_M$ ) are determined.  $C_D$  value represents efficiency and  $C_M$  value represents maneuverability. A more detailed description of this process is given in sec 3.3.

Origami analysis is divided into two categories: Available Area for Solar Cell calculation and Available Inner Volume calculation. Both procedures use the origami method introduced in sec 3.2 and the available Inner Volume calculation is calculated using Rhinoceros as introduced in sec 3.5.

Output data and input data for each process are shown in Fig. 4. Surface data using NURBS was transferred in igs form. Based on this, two-dimensional surface mesh data was provided in origami code and Ansys in inp format. Here again, a three-dimensional mesh was generated in msh format and finally provided to Fluent. Based on this modeling data, the final output data in the form of xls was generated.

This composition of various engineering analysis tools is currently being developed and used in many fields, but for automation, it is difficult to integrate and communicate easily. The methods presented above have their meanings as a means to overcome the limitations.

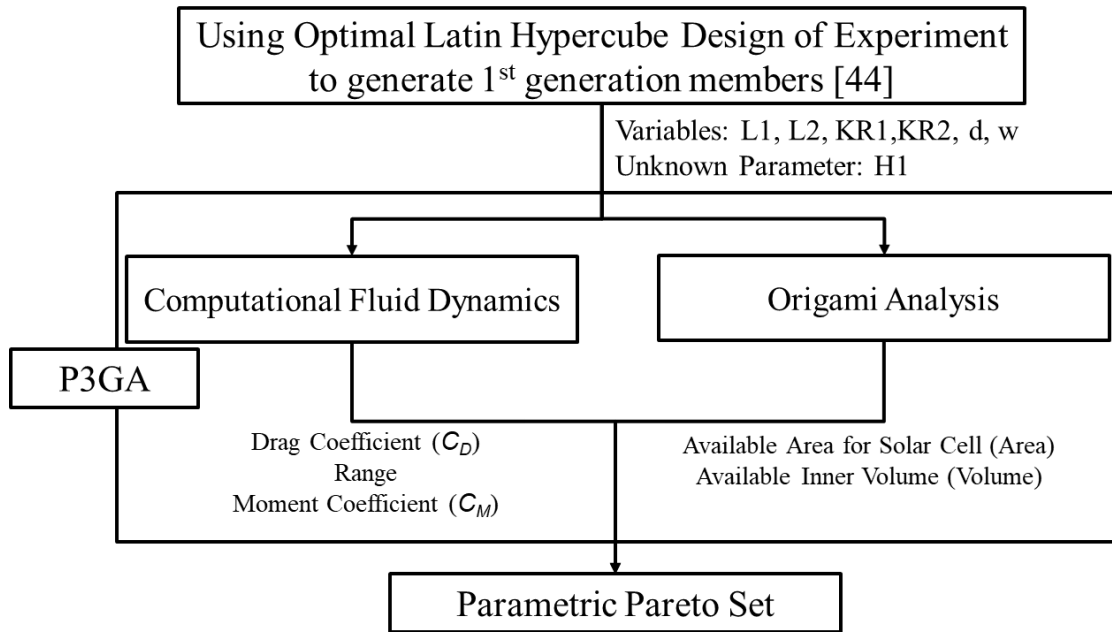


**Figure 4. Overall Design Process**

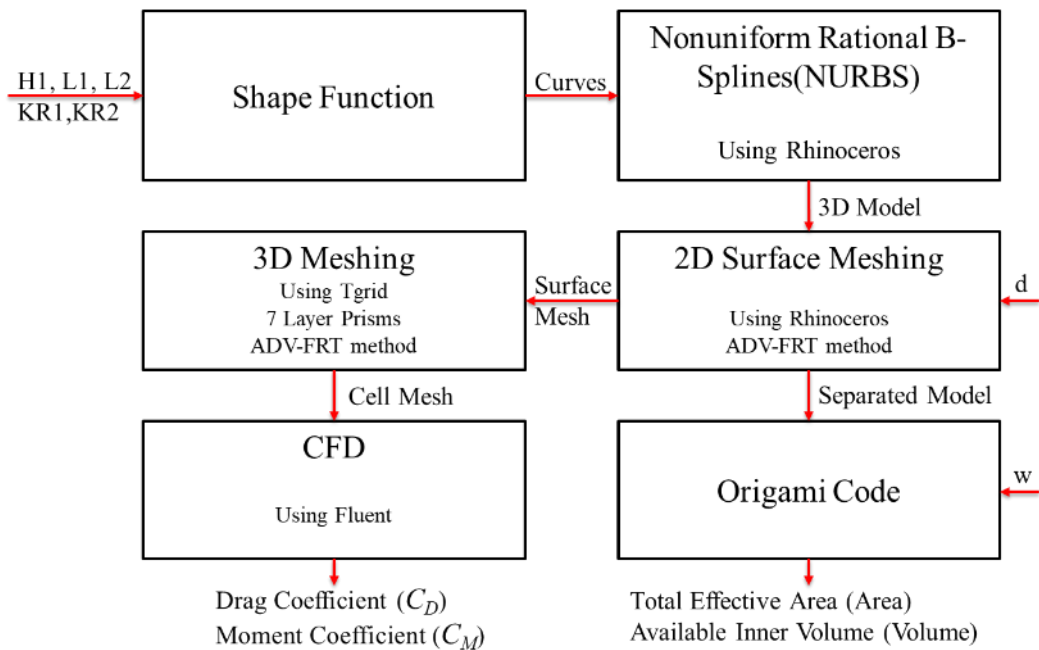


**Figure 5. Flowchart of Analysis Approach**

### 2.3.1. Design of Experiment

Before the optimization, a demonstration of the optimization was performed for evaluation of each objectives. The mathematical expression for the demonstration is as follows:

$$\text{Minimize}_{\mathbf{x}} \quad F(\mathbf{x}, H1) = [C_D; -C_M; -Area]$$

$$\text{Where} \quad \mathbf{x} = [L1, L2, KR1, KR2, w, d]$$

$$\text{Unknown Parameter} = H1$$

$$\text{Subject to} \quad 0.7\text{m} \leq H1 \leq 1.3\text{m}$$

$$0.7\text{m} \leq L1 \leq 1.3\text{m}$$

$$2.2\text{m} \leq L2 \leq 3.8\text{m}$$

$$0.5 \leq KR1 \leq 1.1$$

$$0.7 \leq KR2 \leq 1.3$$

$$0.25\text{m} \leq d \leq 0.75\text{m}$$

$$0.2 \leq w \leq 0.4$$

Variables fall into three categories. First,  $H1$ ,  $L1$ , and  $L2$  are dimensional variables. These variables specify overall sizes. Second,  $KR1$  and  $KR2$  are shape variables used in shape functions. The method using these variables is explained in sec 3.1. Third,  $d$  and  $w$  are variables for origami modeling.  $d$  is the characteristic length of the mesh faces, which is introduced in sec 3.2 and  $w$  is the characteristic length of the tucked regions in the origami design which is introduced in sec 3.5.

### 2.3.2. Optimization for Performance

The performance of the AUV can be evaluated by available inner volume (*volume*) and mission range (*range*). The available inner volume decides the capacity of the AUV for experimental devices, battery, etc. Volume is critical for functional expandability.

The overall design process is as follows:

$$\text{Minimize}_{\mathbf{x}} \quad F(\mathbf{x}, H1) = [-\text{Range}; -\text{Inner Volume}]$$

$$\text{Where} \quad \mathbf{x} = [L1, L2, KR1, KR2, w, d]$$

$$\text{Unknown Parameter} = H1$$

$$\text{Subject to} \quad 0.7\text{m} \leq H1 \leq 1.3\text{m}$$

$$0.7\text{m} \leq L1 \leq 1.3\text{m}$$

$$2.2\text{m} \leq L2 \leq 3.8\text{m}$$

$$0.5 \leq KR1 \leq 1.1$$

$$0.7 \leq KR2 \leq 1.3$$

$$0.25\text{m} \leq d \leq 0.75\text{m}$$

$$0.2 \leq w \leq 0.4$$

### 3. ANALYSIS AND OPTIMIZATION TOOLS

#### 3.1. Three-dimensional Modeling based on Shape Function

A three-dimensional shape of the AUV's outer surface is generally streamlined and very complex, and often varies according to its use and operational environment. To represent the characteristics of the three-dimensional shape configurations in terms of categories, Calkins and Chan [37] classified automobiles into one-box, two-box, three-box, etc. In each category, the boxes, which comprise the shape of the automobile, are divided into section boxes in order to use analytical functions to represent the shape. This method of decomposition is used in automobile structural design [38]. An automobile configuration must meet spatial requirements, also referred to as the package layout [39], including dimensions for the whole body length and width, engine location, space for the driver, roof and trunk, size of the intake, and front and rear glass. The entire outer shape of the automobile is determined by a combination of these principal dimensional variables. Details and attached parts such as bumpers, shoulders, and internal flows can be represented by dividing the section boxes into smaller parts. The same process is adapted for this study. Same as a divided automobile, the AUV is divided into 2 boxes as shown in Fig. 6. The front box is contains the frontal section of the AUV that is obtained by revolving front curve. The AUV region contained in the rear box is determined by rear curve and two straight curves.

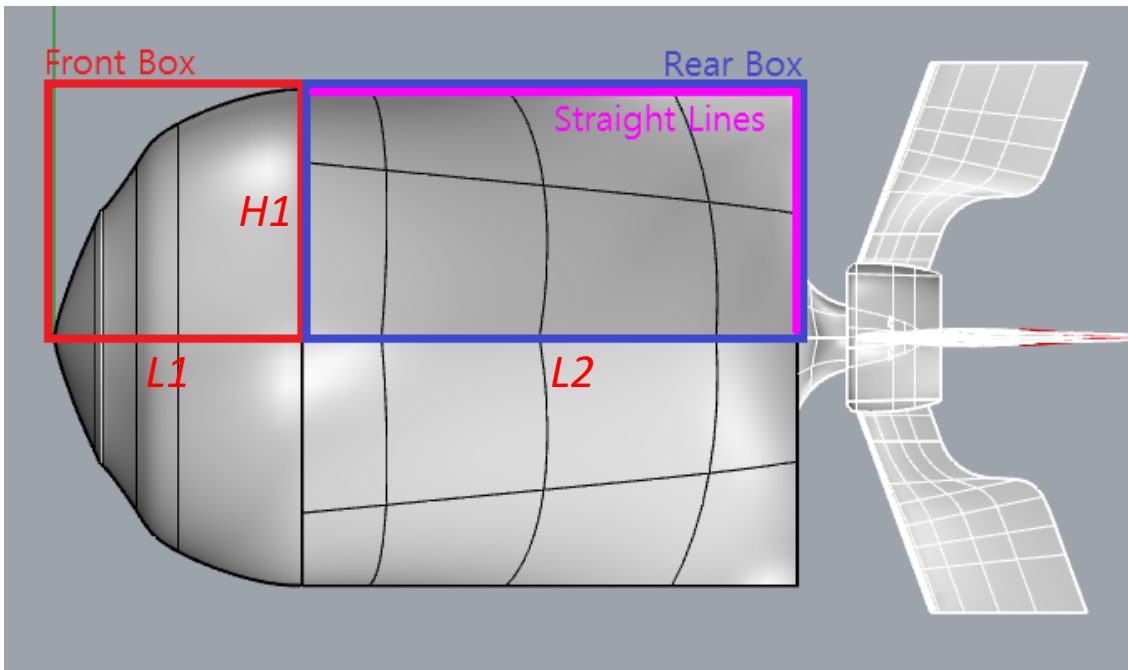
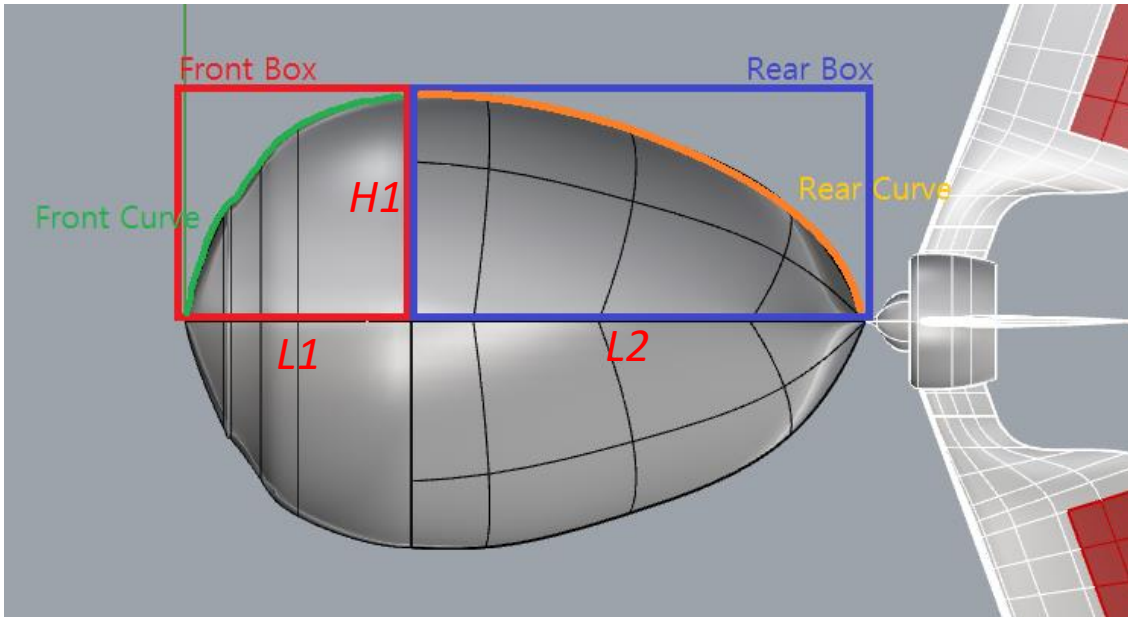


**Figure 6. Side View and Top View of The AUV Shape and Brief Description of Dimension Parameters**

The curves representing the streamlined outer surface of a vehicle can be represented using the following function:

$$F\left(\frac{x}{c}\right) = \left(\frac{x}{c}\right)^{A_1} \left(1 - \frac{x}{c}\right)^{A_2} S\left(\frac{x}{c}\right) + \left(1 - \frac{x}{c}\right) Y_1 + \left(\frac{x}{c}\right) Y_2 \quad (1)$$

where  $x$  and  $c$  are the dimension and length of each section box depicted in Fig.6.

The section function  $S(x/c)$  provides higher flexibility in the design of the shape [22]. The modified functions for AUV case considered in this work are given as follows:

$$\text{Front Box: } \frac{z}{c}\left(\frac{x}{c}\right) = \left(\frac{x}{c}\right)^{0.5} \left(1 - \frac{x}{c}\right) \left[ KR_1 * \left(1 - \frac{x}{c}\right) + \frac{1}{KR_1} * \left(\frac{x}{c}\right) \right] + \left(\frac{x}{c}\right) R_1 \quad (2)$$

$$\text{Rear Box: } \frac{z}{c}\left(\frac{x}{c}\right) = \left(\frac{x}{c}\right)^{0.5} \left(1 - \frac{x}{c}\right) \left[ KR_2 * \left(1 - \frac{x}{c}\right) + \frac{1}{KR_2} * \left(\frac{x}{c}\right) \right] + \left(1 - \frac{x}{c}\right) R_1 \quad (3)$$

Where  $KR1$  and  $KR2$  are design variables that decide the overall shape and  $R1$ , which is equal to  $H1$ , is radius of the revolving circle located between front box and rear box.

And as both equations contain  $R1$  as common value, they have same value at the point they meet. The difference between the models according to the variables is shown in the figure below. The example of  $H1$ ,  $L1$ , and  $L2$  in modeling is shown in Fig.7.

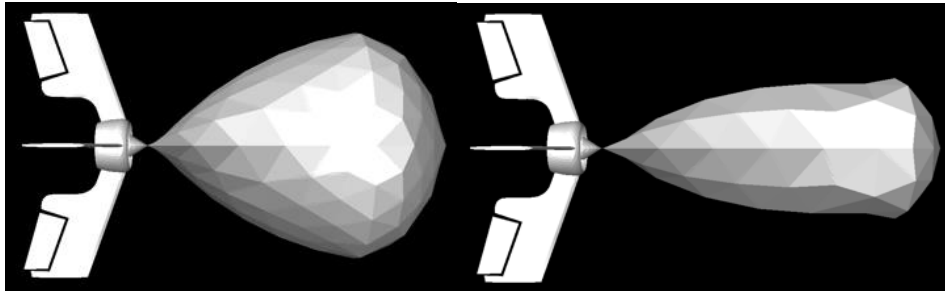


**Figure 7. AUV Model with  $H1=1.27$  m,  $L1=1.05$  m,  $L2=3.3$  m (LEFT) and  $H1=0.72$  m,  $L1=0.85$  m,  $L2=3.74$  m (Right)**

### 3.2. Origami Modeling

The advancing front method [40,41,42,43,44] is utilized here to determine a mesh discretization of the AUV surface (see Fig. 8). Advancing Front Techniques begins with the discretization of geometry boundaries in a two-dimensional corner set. These edges form the outgoing front face to the field. A specific edge of this face is selected and a new triangle is formed based on this edge by combining the two ends of the current edge with the newly created point or the existing point on the face. The current edge is removed from the front because it is currently hidden by the triangle. Likewise, as shown in Fig. 8, the remaining two corners of the new triangle are either assigned to the front or removed from the front, depending on their visibility. Thus, the front can be removed or removed from the stack where the stack, or priority queue, is configured and edges are added sequentially. When the stack is empty, that is, when all the faces are merged together and the domain is completely covered, the process is terminated. One important feature of these methods is the placement of new points. When creating a new triangle, the new point is placed first in the determined location to be the optimal size and shape triangle. The parameter defining this optimal triangle as a function of field position is obtained by a predetermined field function, which may be interpolated from the background grid. Triangles created with new points can be rejected because they can cause crossovers with other front edges. This is determined by calculating the intersection with the near front edge. Alternatively, the existing point on the front can be

located very close to the new point by chance, so it can be used as the point of forming a new triangle to avoid the emergence of a triangle with a few edges later on.

Therefore, existing candidate points are searched for all "near" front points. Therefore, one of the advantages of this approach is the automatic point placement strategy, which typically produces high quality elements in most of the flow fields due to the optimal placement of these new points. In addition, all actual work performed has local characteristics. That is, a cross check is performed with a similar length of neighboring edges to reduce the probability of a round-off error induced failure. Finally, boundary integrity is guaranteed because the boundary heterogeneity constitutes the initial condition. [45]

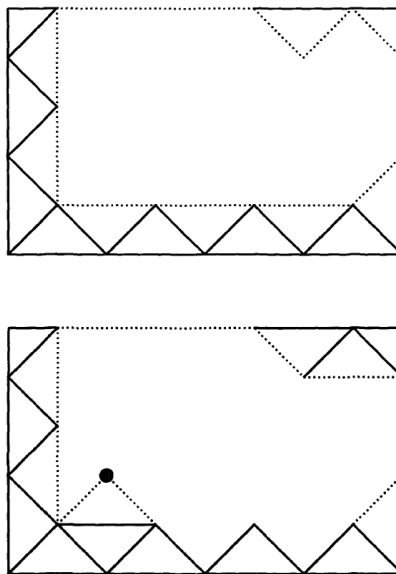


**Figure 8. An illustration of an existing advanced front mesh generation concept in two dimensions. The dotted line indicates the current front. The new triangle is created one at a time by joining the two leading edges to the newly created point or existing lead**

This Advancing Front Meshing technique is applied to determine an origami sheet design that can be folded towards the AUV shape. A uniform mesh size distribution is assumed for this problem and therefore only one characteristic length is required to generate a mesh using the advancing front method. Such a characteristic length was designated as variable “d” in the design process. A mesh generated through the advancing front method is shown in Fig. 9.

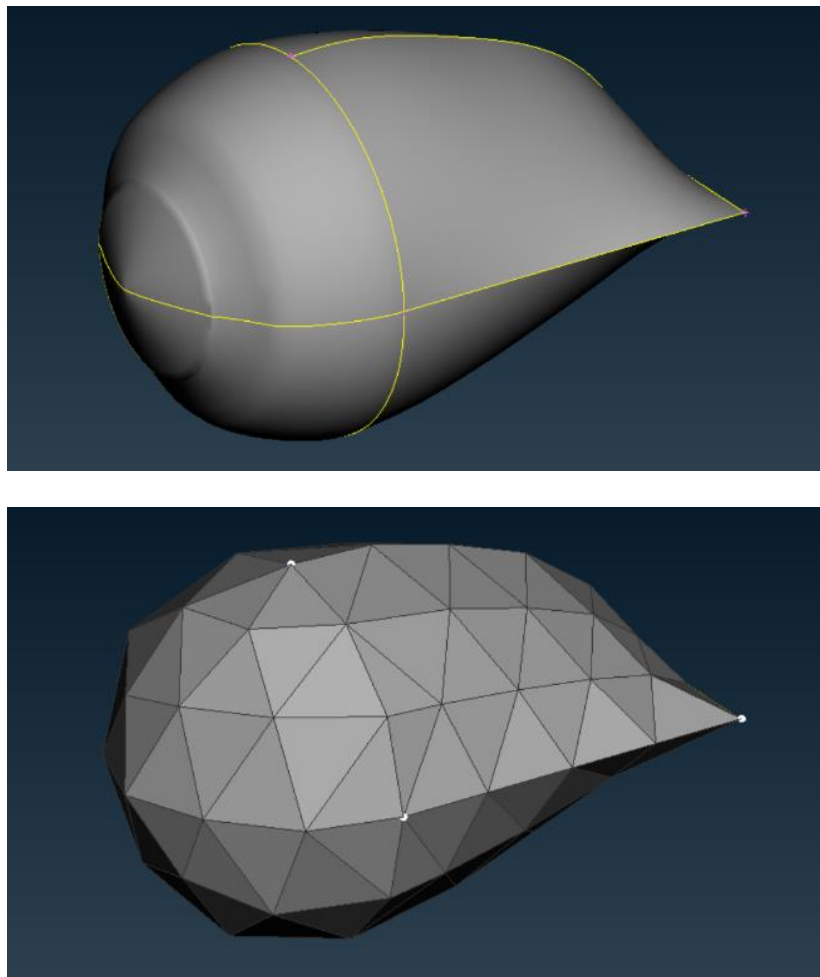


**Figure 9. Three-Dimensional Model Before Meshing (Top) and After Meshing (Bottom)**

### 3.3. Computational Fluid Analysis

A commercial tool ANSYS used for fluid analysis of each case. Boundary condition was 5m/s for velocity, water, and 0.0001 for residual convergence. The basic viscous model is k-epsilon with standard near-wall function of ANSYS. I also used Simple C pressure-velocity coupling technique. Outputs from the analysis are Drag Coefficient ( $C_d$ ) and Moment Coefficient ( $C_m$ ) which are the objectives of optimization process itself.

In this study, CFD analysis was performed using a standard k-e model. Using a two-equation turbulence model, you can solve two separate transport equations to determine turbulence length and time scale. The standard  $k-\varepsilon$  model of ANSYS Fluent belongs to this type of model, Launder and Spalding [46] has become a key element in the computation of practical engineering flows. Robustness, economics, and reasonable accuracy for a wide range of turbulence illustrate its popularity in industrial flow and heat transfer simulations. This is a semi-empirical model, and the derivation of model equations depends on phenomenological considerations and empiricism.

Standard  $k-\varepsilon$  models [46] is a model based on model transport equations for turbulent kinetic energy and its dissipation rate. The model transport equation for  $k-\varepsilon$  is derived from the exact equation, but the model transport equation for  $\varepsilon$  is obtained using physical reasoning and is not nearly identical to the mathematically correct response [47]

The governing equations of  $k$ - $\varepsilon$  is based on three dimensional time dependent compressible Navier-Stokes equations [48]. The conservation laws of mass, momentum, and energy and the equation of state for a perfect gas expressed in terms of Reynolds density-averaged variables and compact tensor notation for  $j=1,2,3$  are

$$\text{Mass Conservation:} \quad \frac{\partial \rho}{\partial t} + \frac{\partial}{\partial x_j} (\rho u_j) = 0$$

$$\text{Momentum Conservation:} \quad \frac{\partial \rho u_i}{\partial t} + \frac{\partial}{\partial x_j} (\rho u_j u_i + p \delta_{ij} - \tau_{ij}) = 0$$

$$\text{Energy Conservation:} \quad \frac{\partial e}{\partial t} + \frac{\partial}{\partial x_j} (u_j (e + p) - u_i \tau_{ij} - q_j) = 0$$

These equations require the definition of the turbulent Reynolds stresses in terms of known quantities [49]. The stress tensor is modeled as proportional to the mean strain-rate tensor, and the factor of proportionality is the eddy viscosity for eddy viscosity models. Reynolds stresses are

$$\tau_{ij} = 2\mu_t \left( S_{ij} - \frac{S_{nn} \delta_{ij}}{3} \right) - \frac{2\rho k \delta_{ij}}{3}$$

$$\text{where} \quad S_{ij} = \frac{1}{2} \left( \frac{\partial u_i}{\partial x_j} + \frac{\partial u_j}{\partial x_i} \right)$$

$$\text{and} \quad \mu_t = \frac{c_\mu f_\mu \rho k^2}{\varepsilon}$$

where  $\mu_t$  is the eddy viscosity,  $S_{ij}$  is the mean-velocity strain-rate tensor,  $\rho$  is the fluid density,  $k$  is the turbulent kinetic energy,  $\delta_{ij}$  is the Kronecker delta, turbulent dissipation rate,  $\varepsilon$ , model coefficient,  $c_\mu$ , is determined by equilibrium analysis at high Reynolds

numbers, and the damping function,  $f_{\mu}$ , is modeled in terms of a turbulence Reynolds

number,  $Re_{\mu} = \rho k^2 / \epsilon \mu$ . [50]

### 3.4. Available Solar Area Calculation

Solar panel, which is adapted in the recent industry, is applied by composition of normalized solar cells. The dimensions of normalized solar cells are 156 mm by 156 mm by 35 mm [51]. As a result, the size of each origami pieces should be larger than the size of single solar cell. Furthermore, the shape of origami pieces in this thesis is triangular. Thus, as shown in Fig.10, for example, the spaces are inevitable to attached square shaped solar cell on the origami pieces. In this research, available solar area calculation is based on assumption that each origami pieces are equilateral triangles. As a result, the available area for solar cells is simply calculated by substituting certain area, which is same as the 1.5 times area of single cell, and the available area of origami piece smaller than that is calculated as zero.



**Figure 10. Example Of Triangular Solar Panel, Adapted from [52]**

### 3.5. Available Inner Volume Calculation

As introduced in Section 2.4, during the creation of the origami surface, a tucked surface is created. All surface triangles are isometric and the molecules at the edges are symmetrical. As shown in Fig.11, the composition of the molecular mesh can be represented by the distance and angle of the edge folding molecule.

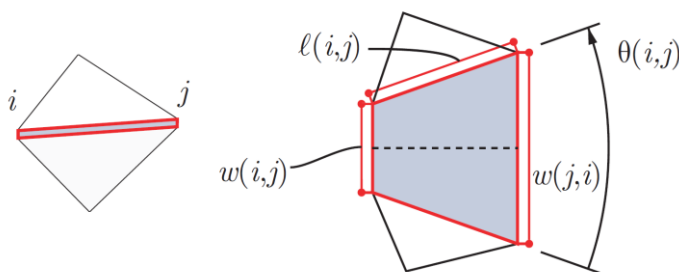


**Figure 11. Edge-tucking molecule is represented in terms of two parameters:  $w$  and  $\theta$ , Adapted from [53]**

For an adjacent pair of vertices  $i, j$ , the angle  $\theta(i, j)$ , between the edges of a pair corresponding to  $ij$ , is assigned a sign according to the direction of rotation relative to the vertex  $i$ . The width  $w(i, j)$  is defined as the signed length of the edge on the boundary of vertex-tucking molecule corresponding to  $i$  shared by edge tucking molecule corresponding to  $ij$ . Negative value indicates that the molecule is crossed or flipped. Edge tucking molecules are represented by isosceles trapezoids as follows,

$$\theta(j, i) = -\theta(i, j)$$

and

$$w(j, i) = w(i, j) + 2l(i, j) \sin\left(\frac{1}{2}\theta(i, j)\right)$$

where  $l(i, j)$  is the length of edge  $ij$ . Assume nominal vertex  $o$  represents the boundary. And let  $j_n$  ( $n = 0, \dots, N-1$ , where  $N$  is the valency of vertex  $i$ ) denote the vertex which is adjacent to vertex  $i$  or boundary  $o$  connected counterclockwise in this ordering. And  $\alpha(i, j)$  denote the sector angle on  $S$  between  $ij_{n-1(\text{mod}N)}$  and  $ij_n$ . Thus, the equality conditions adjacent to vertex  $i$  are given as follows.

$$\sum_{n=0}^{N-1} \theta(i, j_n) = 2\pi - \sum_{n=0}^{N-1} \alpha(i, j_n)$$

and

$$\sum_{n=0}^{N-1} w(i, j_n) \begin{bmatrix} \cos(\sum_{m=1}^n \vartheta_m) \\ \sin(\sum_{m=1}^n \vartheta_m) \end{bmatrix} = \begin{bmatrix} 0 \\ 0 \end{bmatrix}$$

Where  $\vartheta_m$  is external angle between the adjacent edges of tucking molecule. As shown in Fig.12,  $\vartheta_m$  is given by,

$$\vartheta_m = \frac{1}{2}\theta(i, j_{m-1}) + \alpha(i, j_m) + \frac{1}{2}\theta(i, j_m)$$

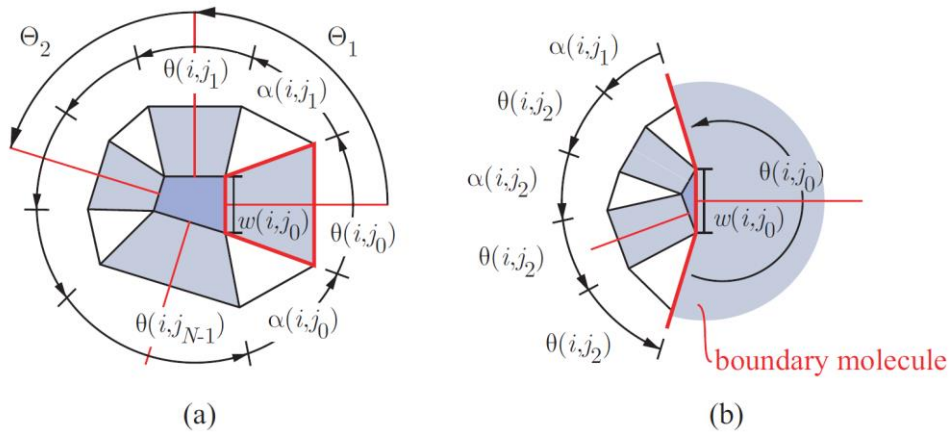


**Figure 12. (a) Vertex-tucking molecule surrounded by polygons and edge-tucking molecules. (b) Vertex-tucking molecule on the boundary, Adapted from [53]**

Due to the tucked surface, as shown in Fig. 13, the difference between the volume calculated from initial outer surface and the real volume available occurred. To calculate this volume, many methods were applied. The first method I have tried was shifting outer surface in orthonormal direction. However, in the process of moving the surface, a shrink occurs. As a result, a surface break occurred, which results in an open volume. Since the volume cannot be calculated, I decided not to adopt this approach. Another method is shifting the outer surface in uniform direction. But it is also not selected because there is a difference from the actual available Inner Volume.

To calculate this, I need to recreate the available imaginary inner surface, not the actual outer surface of origami, to calculate the volume. To do this, I have created a surface based on the center point of each bended surface. To make the surface, I used the 'mesh from points' function provided by the Rhinoceros program for surface creation. The method is based on adjacent points which is an approximation calculated by taking the square root of the quotient of the area of the bounding box divided by the number of points [54]. By connecting the points in a triangular shape, meshed surface is created. Since all the surfaces are created in planar shape, it is easily changed into NURBS surface which forms a closed volume.

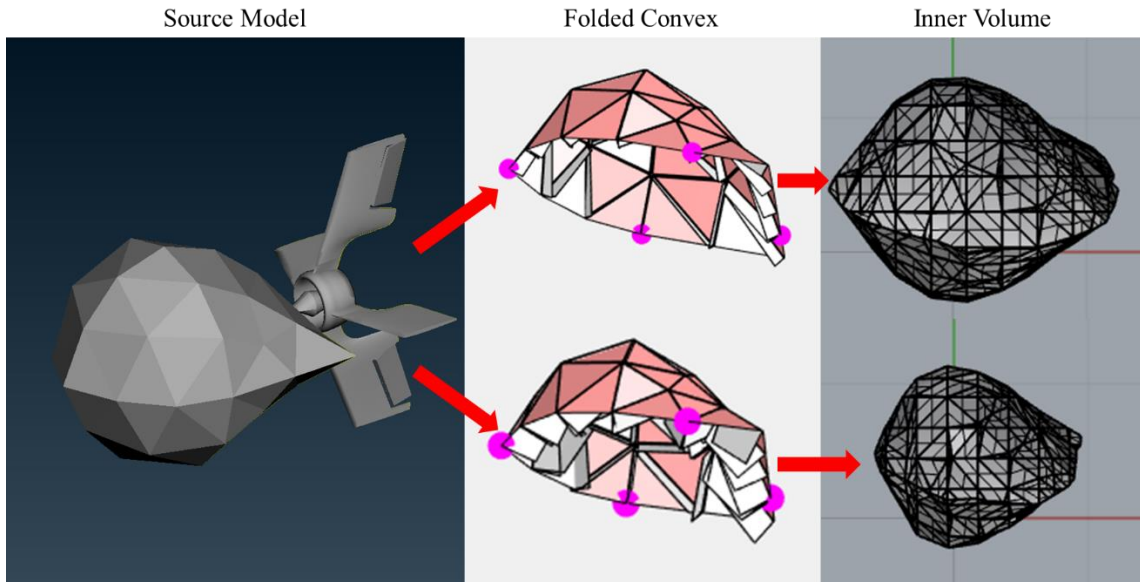


**Figure 13. Comparison of Same Model With Different w Value. Same model with  $w=0.2$  (Top, Available Inner Volume =  $2.497 \text{ m}^3$ ) and  $w=0.6$  (Bottom, Available Inner Volume =  $1.165 \text{ m}^3$ )**

### 3.6. Mission Range Calculation

Calculation of mission range is based on several assumptions. Mathematical expression for range is,  $Range = \eta_e \eta_P \eta_M \frac{E_c}{Drag}$ , Where  $\eta_e$ ,  $\eta_P$  and  $\eta_M$  are efficiency of speed controller, propeller and motor.  $E_c$  is collected solar energy by solar cells and Drag is drag force of the AUV. Insolation, the amount of exposure to the sun, is assumed same as the condition of Hawaii in June,  $6000 \text{ Wh/m}^2$  [21,35]. For drag force calculation, drag coefficient ( $C_D$ ) is calculated through ANSYS.

### 3.7. Parametric Optimization using P3GA

An effective approach in the process of optimization is to focus only on the subset of realizations that may be potentially desirable to the decision maker, the system engineer. The concept of parameterized Pareto dominance (PPD) provides a means for identifying potentially desirable members, collectively referred to as parameterized Pareto frontier (PPF) [55]. This criterion is a generalization of the Pareto dominance (CPD) rule to handle situations where the rank of some attributes is not known. The approximation of the PPF differs from the problem of approximating the classic Pareto frontier (CPF) in which there are many multi-objective optimization algorithms such as the appropriate equal constraint condition [56], the regular constraint method, and the regular constraint condition [57]. And general purpose genetic algorithms (MOGAs) such as the Nondominated Sorting Genetic Algorithm II (NSGA II) [58]. In general, PPF cannot be approximated by applying a conventional multipurpose optimization algorithm directly. As a result, previous applications in PPF relied on nondiscretionary substitution techniques to use observational data for engineering components or to generate data using models. A more efficient approach is needed.

The novelty of P3GA is in the use of PPD as the dominance criterion and the concept of predicted dominance. Because many aspects of the algorithm are well documented in the MOGA literature, I only describe the novel portions of the algorithm: (1) determining the predicted feasible set and (2) predicted PPD dominance. These correspond to the shaded processes in Fig. 14. [15].

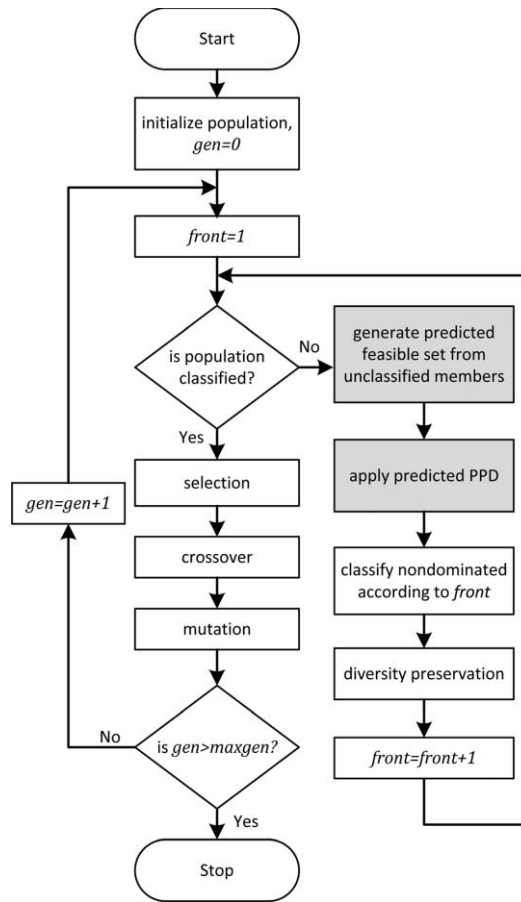


**Figure 14. Flow chart of the P3GA, Adapted from [15]**

Because the application of PPD alone makes it difficult to predict the dominance of all members, dominance analysis is performed not by relying on individual members of the population, but those that are expected to be feasible. To predict what is feasible, the observed points are used. The points that are dominated by the members of the predictable feasible set are the predicted dominant points. To determine the predictable set, P3GA relies on the SVDD technique [59], which models the outer boundary of the current population in the combined variable space of the objective and the parameter. Fig.15 shows the predicted parameterized dominance.

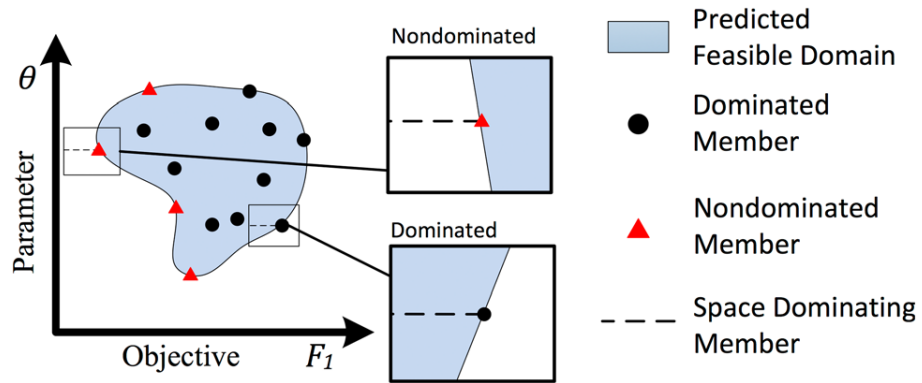


**Figure 15. An illustration of predicted dominance, Adapted from [60]**

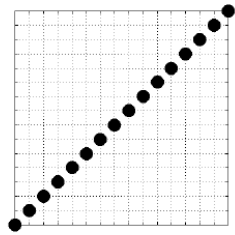
The discrete set of points in the Pareto frontier is parameterized in the output of P3GA. I normalize the data using Kriging interpolation to fit the model of the parameterized Pareto Frontier in the combined space of the property space, the design goal and the parameter variable. Fitting models must be in proper sequence and mathematical form, or interpolated as in Kriging [60,61]

## 4. RESULTS

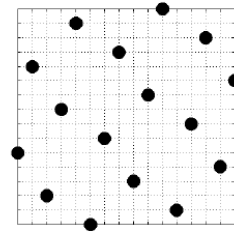
### 4.1. Design of Experiment

In general, design optimization requires large number of expensive simulations. However, as the evolution of the hardware cannot keep pace with the evolution of algorithms, the need for pre-optimization has increased [62]. To reduce the cost of these calculations, a surrogate model, also called as a metamodel, is used instead of the full real simulation model [63,64,65,66,67,68]. Surrogate-based design optimization begins by identifying locations in the design space where the simulation is performed. The process of identifying locations in the design space is known as Design of Experiment (DOE) [69,70]. Especially, Latin hypercube design (LHD) proposed by McKay, Iman and Conover are very famous [71,71].

The advantage of a typical LHD is that the number of samples (points) is not fixed, and the sampling points have high orthogonality [73, 74]. Figure 16 shows two examples of LHDs with  $n_v = 2$  and  $p_n = 16$ . Since the LHD is constructed using random procedures, there is no element that interferes with a design with low space fill quality, as in the extreme case of Figure 16 (a). A better choice is shown in Figure 16 (b), where the points are more uniformly distributed in the domain.



(a)



(b)

**Figure 16. Examples of Latin Hypercube Designs, Adapted from [74]**

Based on these advantages, in the optimization, the 1st generation of p3ga, which was formed randomly until now, was created by using LHD.

The utility of LHD is clearly observed when comparing the first generation of DOE and optimization. As shown in Fig.17, when the initial points are selected randomly, the distribution of each section is jagged. On the other hand, when LHD is selected, the parameters are uniformly spread over all sections. The scattered plot of last generation is shown in Fig.18. The difference of convergence is clearly observed.

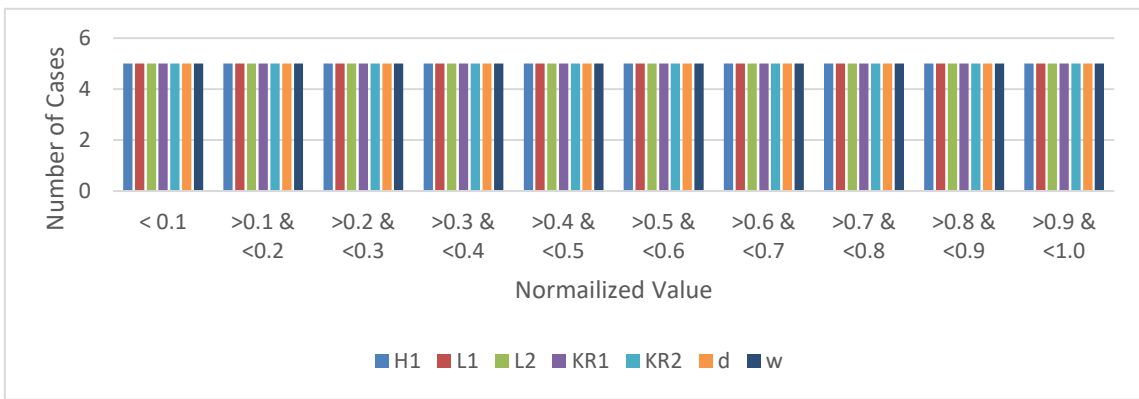
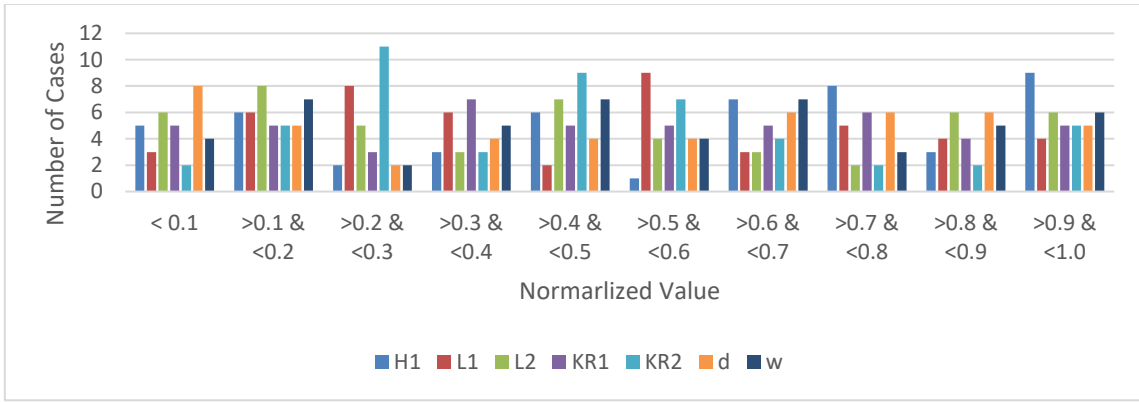


**Figure 17. Distribution of Experimental Points (First Generation), Design of Experiment (TOP), Optimization (BOTTOM)**

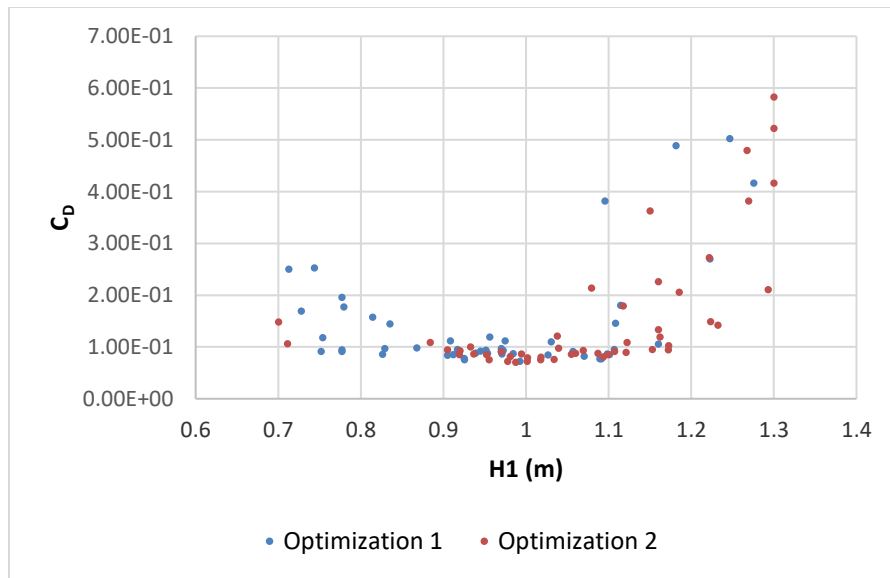


**Figure 18. Experimental Points (25th Generation), H1 vs CD**

## 4.2. Validation of Models

### 4.2.1. Submarine Validation for Mesh

In order to investigate the effect of meshing on the performance of the submarine prior to the full optimization, simulation was performed using the actual submarine model. The base submarine model is a 1/10 scale Typhoon class model, as shown in Fig.19.

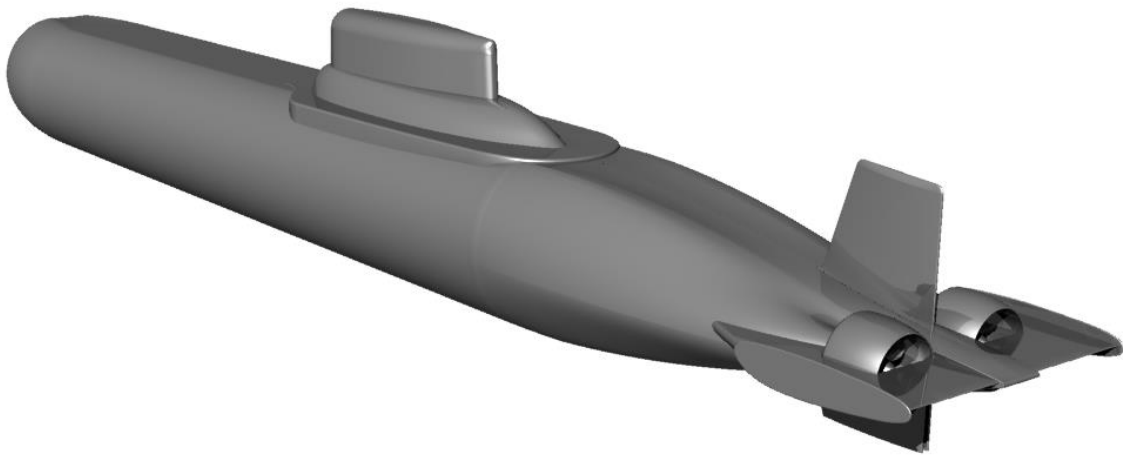


**Figure 19. Base Model – 1/10 Scale Typhoon Type Submarine**

Tail wing for  $C_M$  calculation is shown in Fig.20, a  $45^\circ$  Rudder Angle was used.

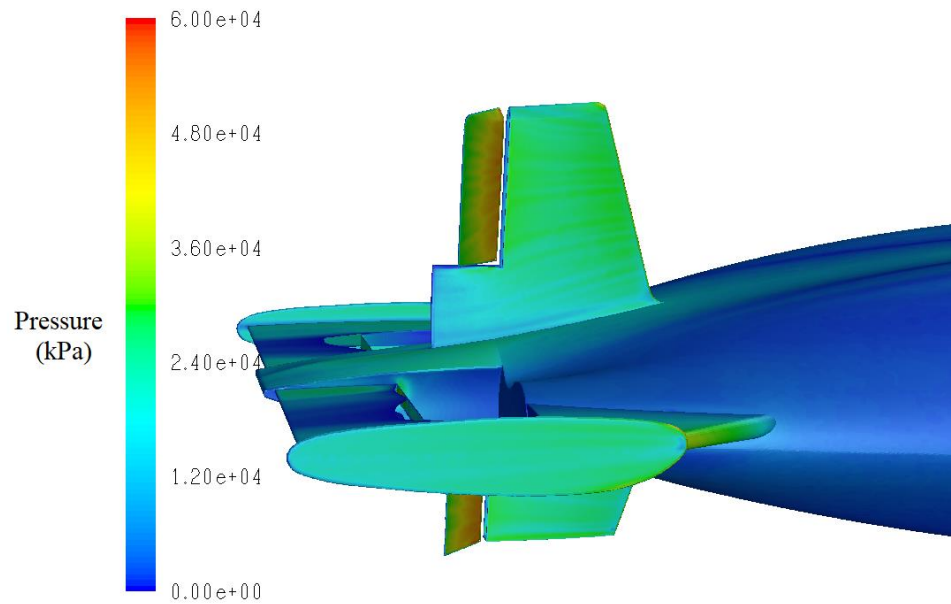


**Figure 20. Maneuvering Case Validation Result**

As a result of the validation, as expected, the  $C_D$  value increased as the size of pieces. This is due to the effect of separation at each edge. As the size of each pieces grows, the edges become sharper, resulting in larger wakes. This property increases the drag and increases the  $C_D$  value. On the other hand, the  $C_M$  value is not directly proportional to the size of the slice, but the origamized model is slightly larger than the smooth base model. To prove the reliability of the CFD analysis, I have made several test cases and compared with existing test result. As shown in the smooth model, the  $C_D$  value of the CFD analysis is similar to the known value. And the trend, large origami elements cause large drag, is also shown in the sphere too.

	Base Model ( $d=0\text{mm}$ )	$d=50\text{mm}$	$d=100\text{mm}$	$d=200\text{mm}$
Drag Coefficient ( $C_D$ )	0.104	0.155	0.346	0.437

Mesh size for CFD Analysis: 10mm

**Table 1. Drag Coefficient of a Sphere relative to Reynolds number, reference figure Adapted from [75]**

	Base Model	Origami Model with Small Pieces	Origami Model with Large Pieces
Number of Front Pieces	0	50	20
$C_D$	7.6023e-02	7.6344e-02	7.9363e-02
$C_m$	3.4365e-02	6.9741e-02	6.7728e-02
Figure			

**Table 2. Validation Results for Origami Piece Size**

#### 4.2.2. Tail Wing

Before performing the simulation, I performed validation for tail wing selection, which will be commonly attached to all models. Two types of tail wings used in the validation is shown in Fig.21. The tail wing of type an exhibited a lower  $C_D$  value but was excluded from this optimization because it is accompanied by the roll direction maneuver during yaw direction maneuver, which is the focus of this study.

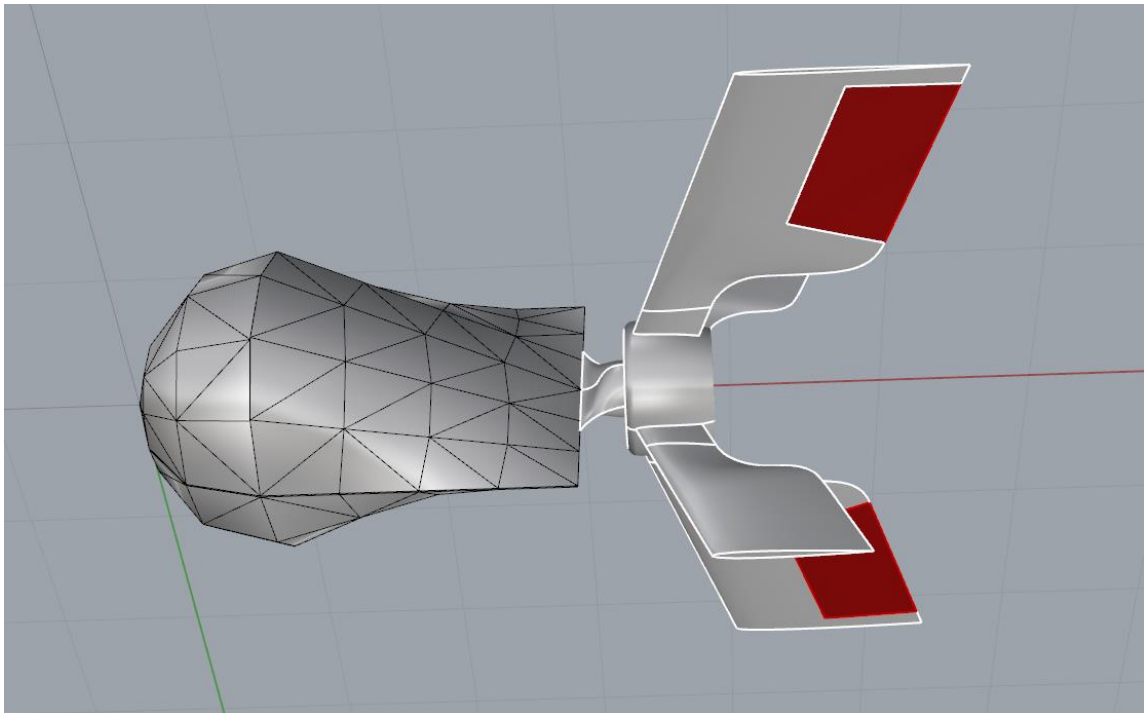
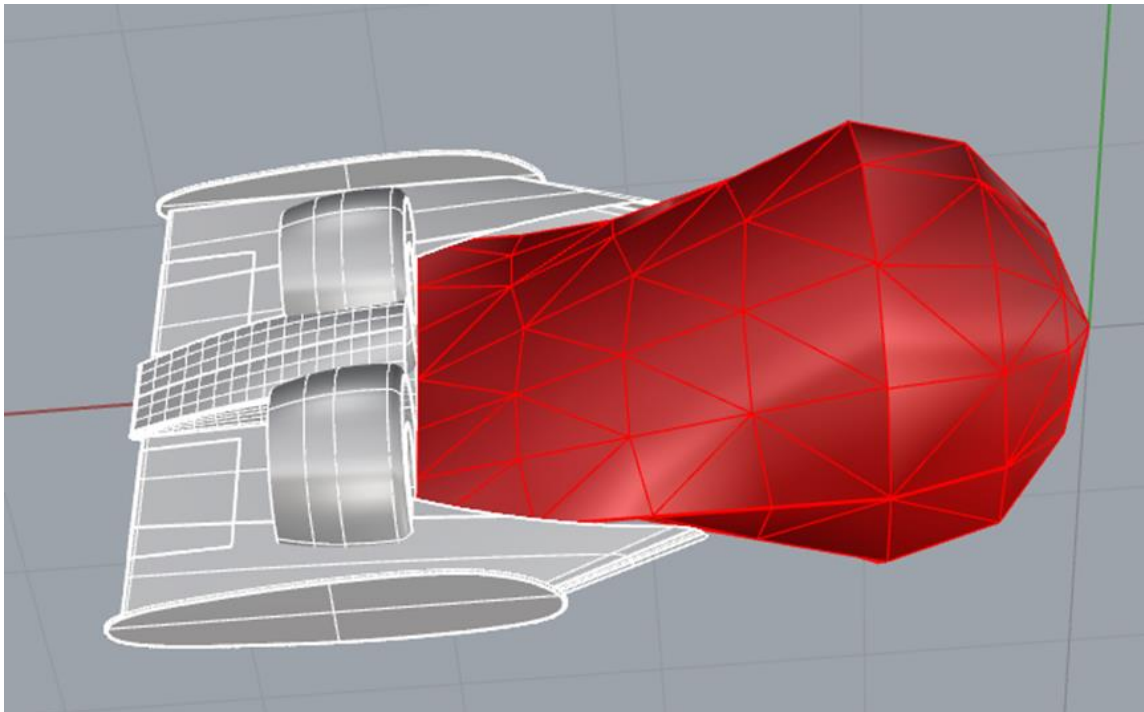


**Figure 21. Two Types of Tail Wings for Validation. A-Type (Top) And B-Type (Bottom)**

### 4.3. Physical Characteristics

As shown in the results of the sensitivity analysis in Fig. 22, the  $C_D$  values are highly affected by input values such as  $H1$  and  $w$ . From the projected results the projected results of the optimization, Fig. 23, there is a certain minimum value that no population member can achieve lower value, about 0.08, than that. Due to the result, this  $C_D$  value can be regarded as characteristic optimal value of this type of AUV. Based on the results of this sensitivity analysis, I set the range of the input value and set the default value in the center of the range to improve the validity of the optimization result.

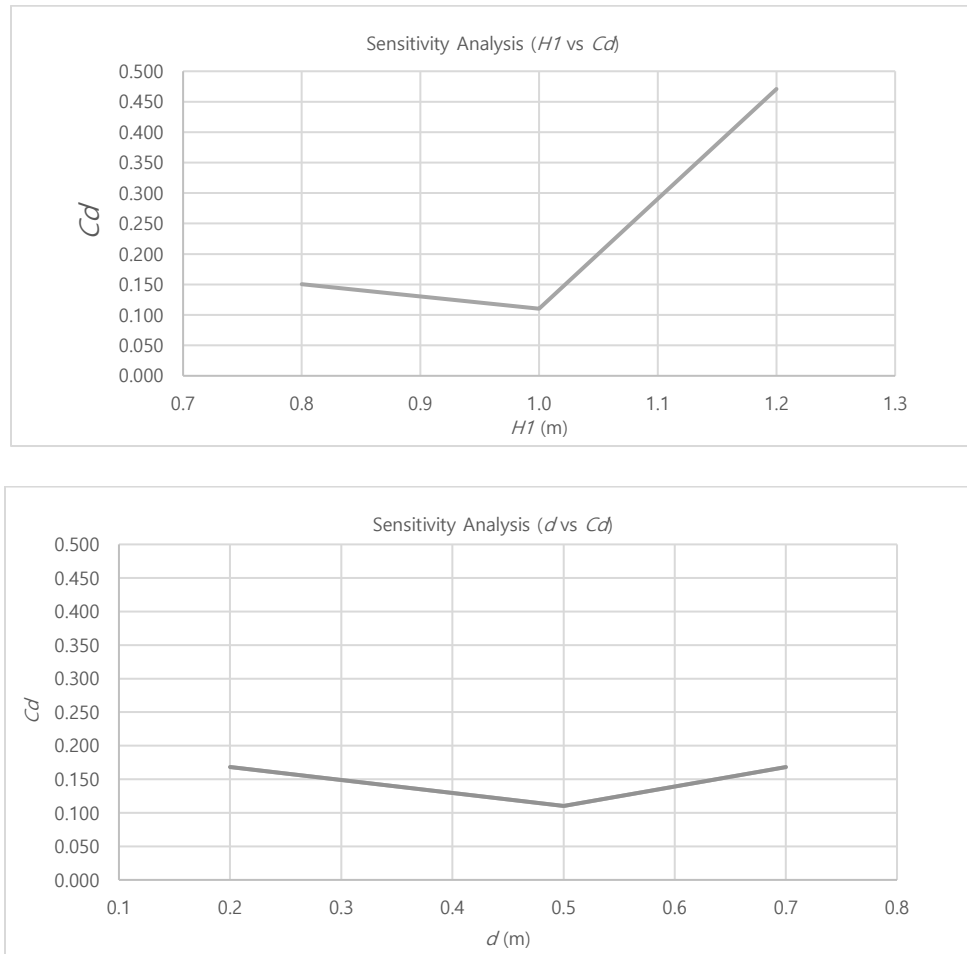


**Figure 22. Results of Sensitivity Analysis. H1 vs CD (Top) and d vs CD (Bottom)**

One unusual point in Fig. 23 is that all the test points appear above a certain  $C_D$  value. This phenomenon is due to the influence of the  $C_D$  value on the Reynolds number, as shown in Table.1. This simulation has a range of  $Re = 10^6 \sim 10^7$  because  $v = 5 \text{ m/s}$  and water are assumed as mentioned above. Therefore, the sphere of the range has a  $C_D$  value of about 0.2 and the minimum  $C_D$  value of about 0.1 for a streamlined AUV. In addition, the reason for the flat result rather than the plot with a positive slope is that the  $C_d$  value is inversely proportional to the projected area, and the projected area is again proportional to  $HI^2$ . As shown in Fig. 23, the result of which is relatively proportional than Fig. 24 is generated. As shown in Fig.24, the Drag Force is proportional to  $HI^2$ . However, as the  $HI$  value increases, the size of the area also increases, and a trade-off occurs between the drag force and the *Available Area*. Based on this result, in Optimization, *Range* other than the *available area* or  $C_D$  was selected as one objective.

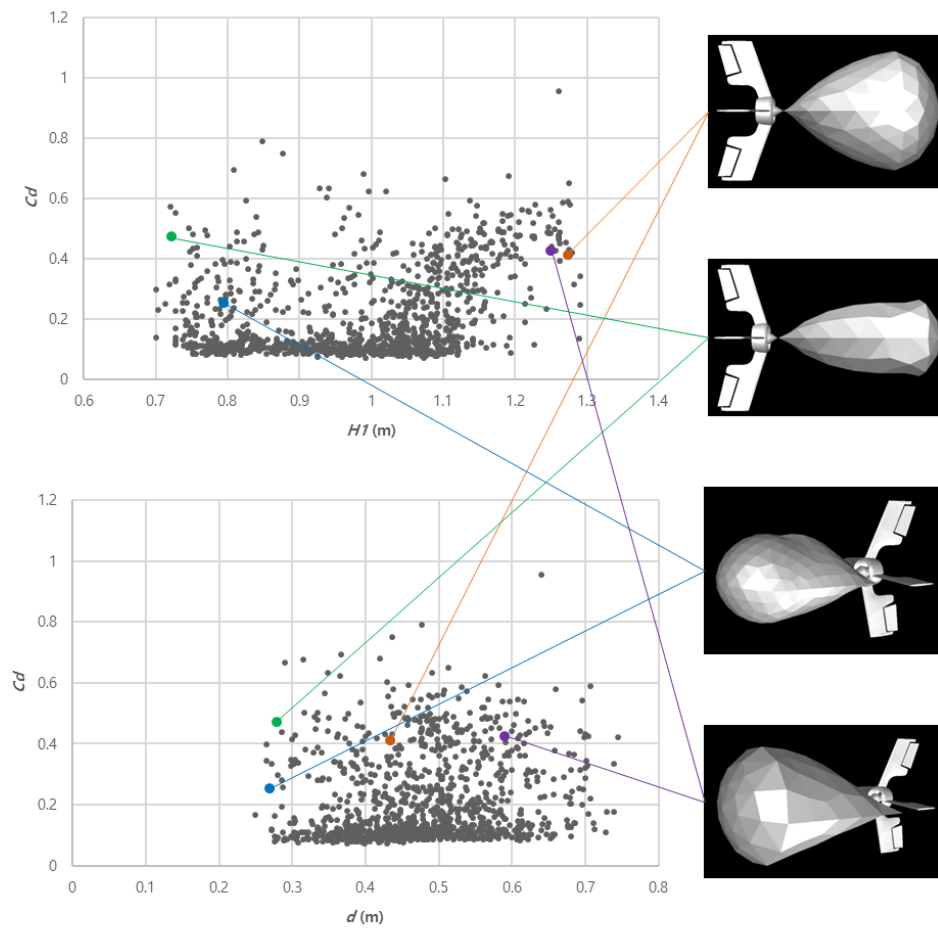


**Figure 23. Projected Scatter Plot of All Populations: H1 vs. CD (Top) and d Vs. CD (Bottom)**

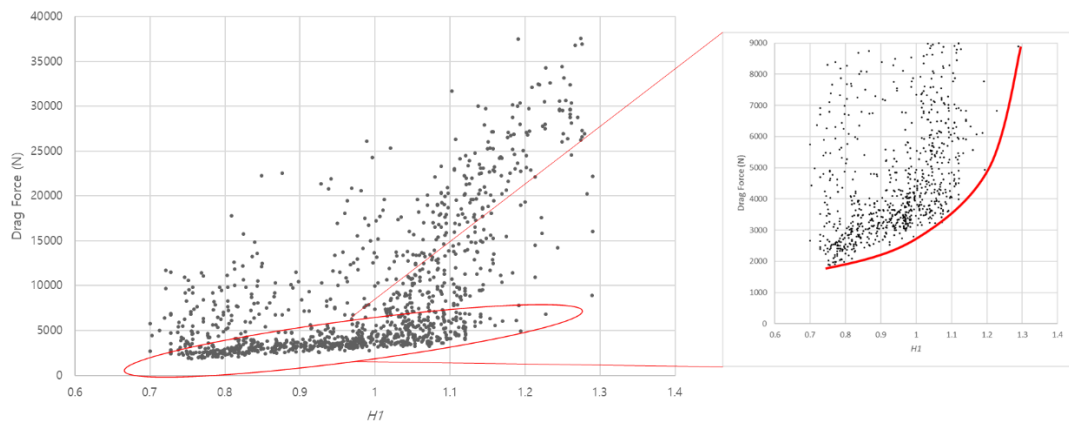


**Figure 24. Projected Scatter Plot of All Populations: H1 vs. Drag Force**

Tendency between available Area for solar panel and  $d$ , is not clear. However, the number of data point with 0 available Area is decreased as the  $d$  increases. In the same manner, tendency between  $w$  and Area is not clear. As shown in Figure 25, there is no observable correlation between  $w$  (the fold width), and Area.

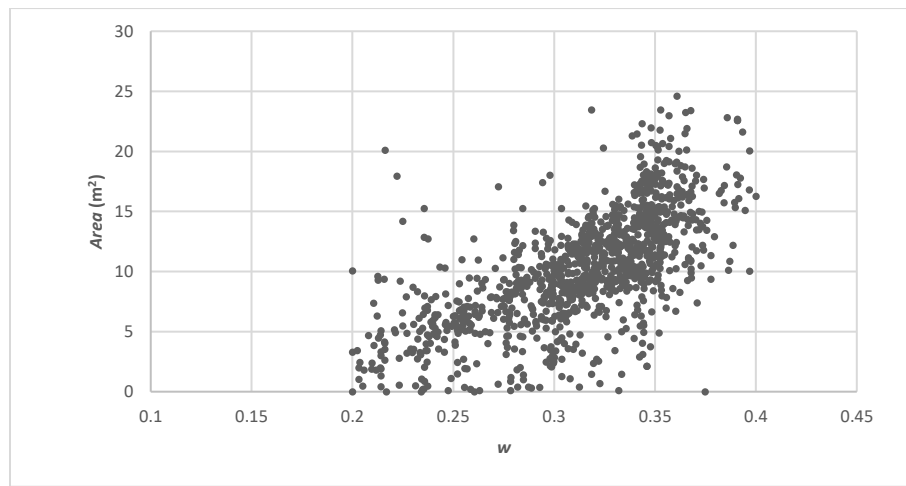


**Figure 25. Projected Scatter Plot of All Populations w vs. Area**

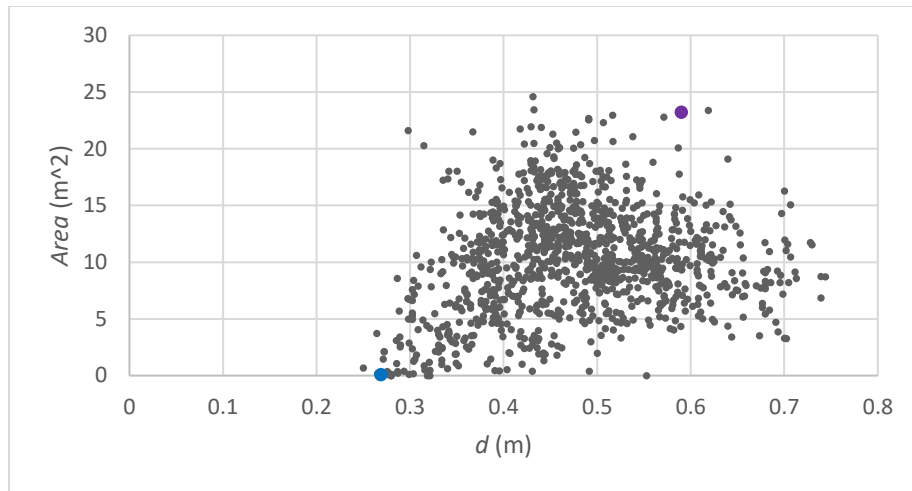


**Figure 26. Projected Scatter Plot of All Populations  $d$  vs. Area**

Similar to the results from sensitivity analysis, tendency between  $H1$  and  $C_M$  is clearly negative. As shown in Fig.26,  $H1$  increases, controllability of AUV decreases. This is caused by difference of projected area.  $H1$  increases both frontal projection area and side projection area. Both areas affect  $C_M$ . Since all the cases shared same tail wings, higher  $C_M$  means higher controllability through moment force.

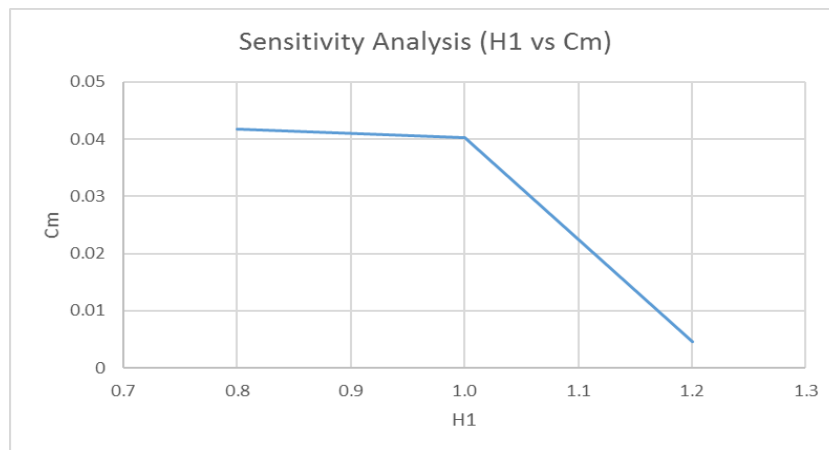


**Figure 27. Results of  $H1$  vs.  $C_M$  from Sensitivity Analysis (Top) and Projected Scatter Plot (Bottom)**

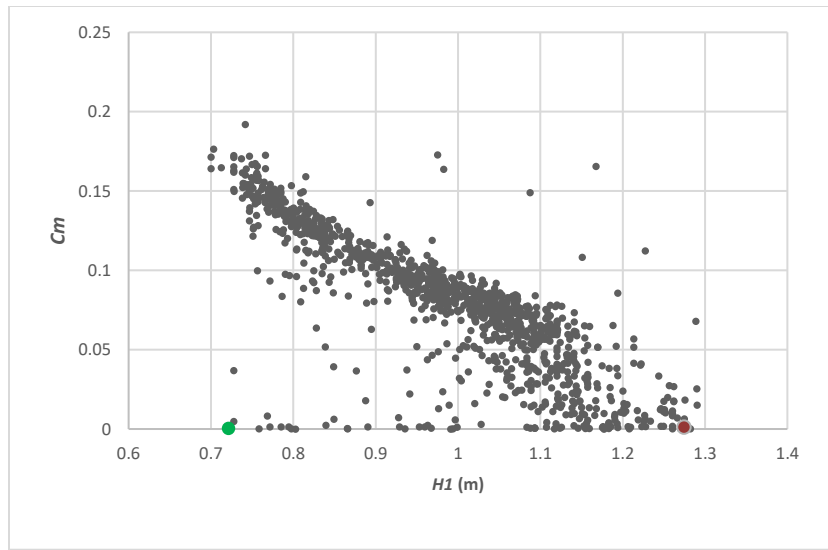


**Figure 27. Continued**

From Optimization, as shown in Fig. 27, tendency between the parameter  $H1$  and *inner volume* and *range* were brought to light. As expected, *inner volume* is directly proportional to  $H1$ . In contrast, the relation between *range* and  $H1$  is not clearly observable as also shown in Fig. 27. Here, the dots in different colors represent the experimental points of the last generation. The distributions are spread over a wide range but show linear results. This is due to the fact that the range is broad because it is projected, but it is close to the formed Pareto front as shown in the three-dimensional plot.

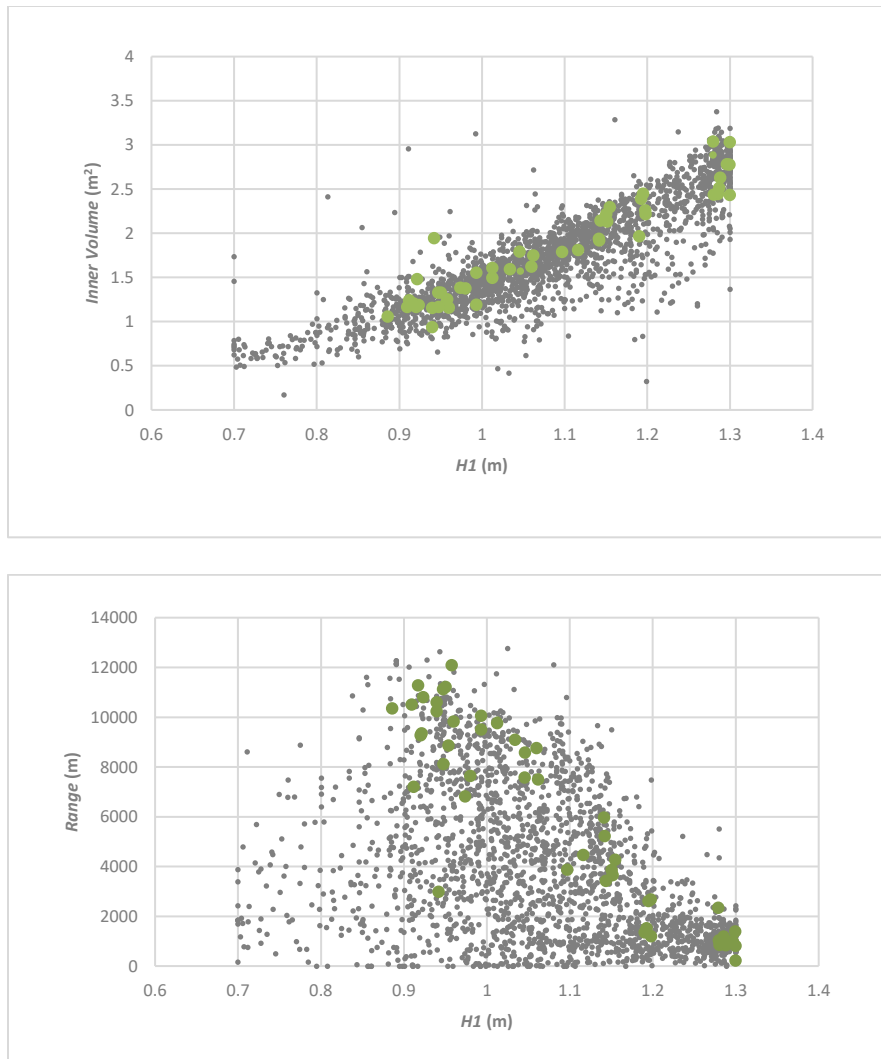


**Figure 28. Projected Scatter Plot of all Populations H1 vs. Inner Volume (Top) and H1 vs Range (Bottom)**

Figure. 28 shows the projected plot of available *inner volume* vs. *range* and their associated Pareto frontier. Range is directly related with the available area for solar cells for solar cells. In contrast, available area and inner volume are inversely proportional due to hidden surfaces. That is the reason that projected Pareto front displays a negative slope. The parameterized Pareto points, shown in bottom of Fig.28, the trend due to H1

is clearly observed. As the H1 increases, Available Inner Volume increase while the Range decreases. This is due to the trade-off between hydrodynamically efficient shape and large inner volume.

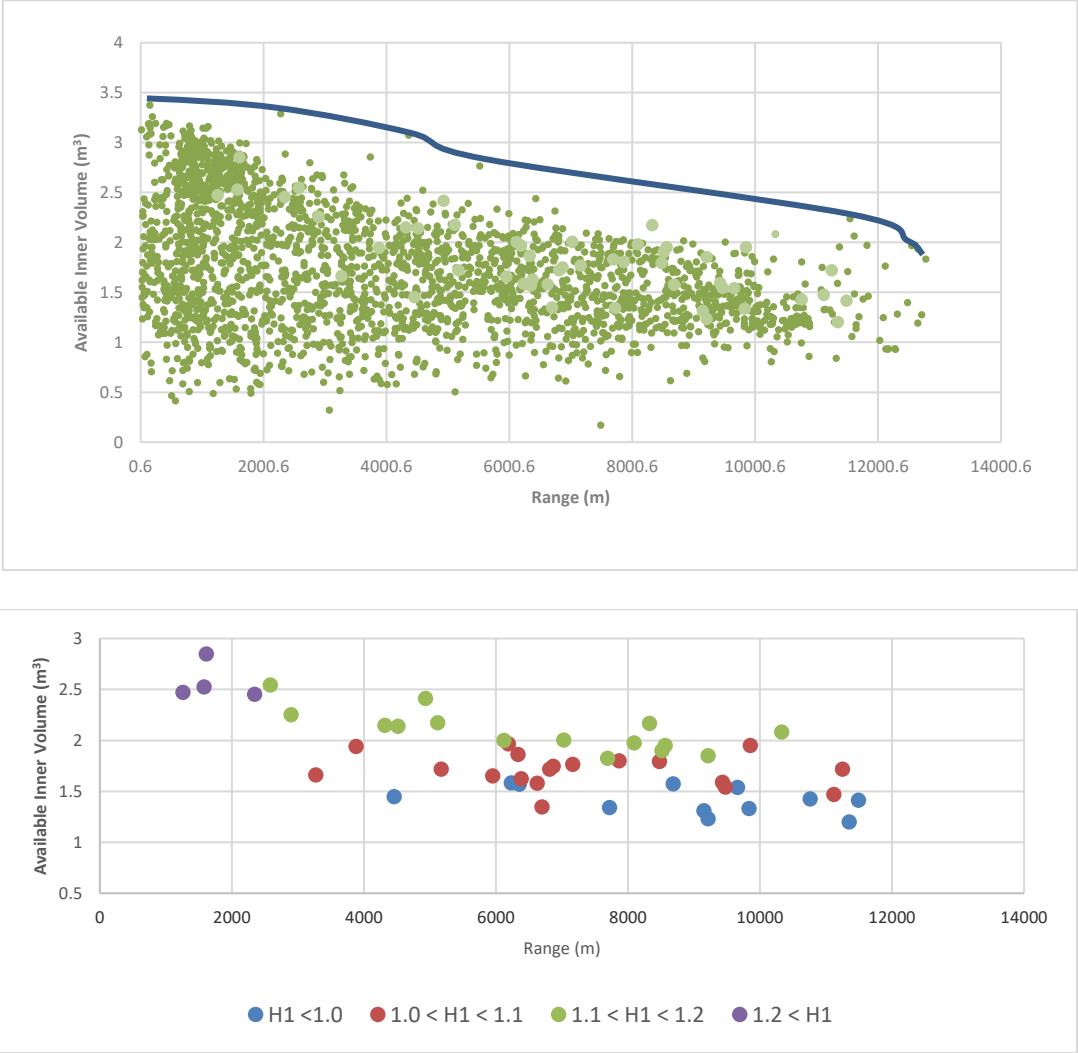


**Figure 29. Projected Scatter Plot for Range vs Inner Volume of all Populations (TOP) and Non-dominated Populations (BOTTOM)**

#### 4.4. Pareto Front

Three objectives and one unknown parameter are considered in Design of Experiment. Therefore, the Pareto frontier forms a surface in three-dimensional space. As shown in Fig. 29, the ranges of scattered points are wide for all objectives. However, the three-dimensional Pareto surface, shown in Fig. 30, is formed in a small range. This is because design points located at the boundaries exhibited desirable results for one of the objectives but not for the others. Another issue to consider from the results is zero available solar cell area for several cases. If the area of each mesh is too small to attach a single solar cell, then the available area is set to zero for the mesh. That is the reason why many points are located on the 0 area line. As shown in Fig. 30, this happened in optimization again as 0 range scattered points.

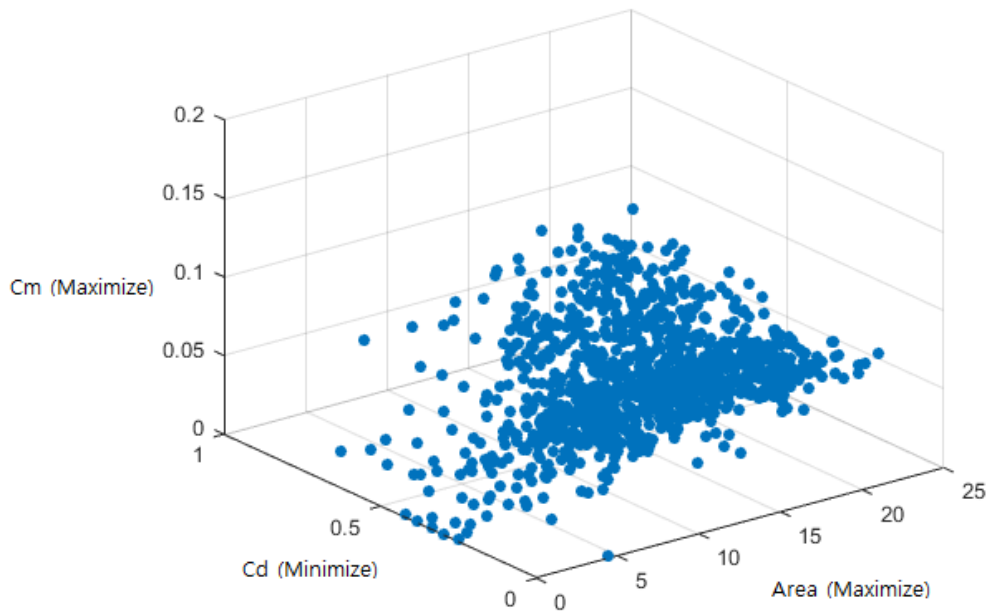


**Figure 30. Three-Dimensional Scatter Plot of all Populations for Design of Experiment**

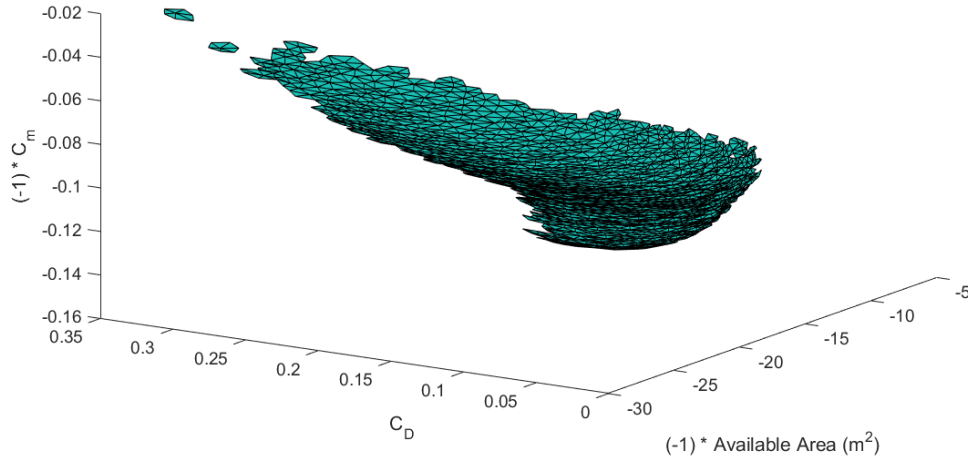


**Figure 31. Three-Dimensional Pareto Frontiers for Design of Experiment**

For the optimization, dependence toward the uncertain parameter  $HI$  is clarified in Fig. 31 and Fig. 32. Similar to the results from Fig. 26,  $HI$  and the *available inner volume* are dependent. And for all parameter, trade-off between two objectives is observed. The feature of the pareto front is that it is not a surface with a gentle slope but a surface with a large slope where the *Inner Volume* changes abruptly. This is due to the difference in the influence of the  $w$  value. The available *Inner Volume* changes greatly depending on the value of  $w$ , but the change of the *Range* is not large, and this phenomenon occurs. As you can see from Fig. 30, the reason why you can show a high range value at the middle value  $HI$  than the maximum and minimum values is due to the range of  $L1$  and  $L2$  values in Optimization # 2. If  $L1$  and  $L2$  values are not limited, the *Range* decreases and the available *Inner Volume* increases as the  $HI$  value increases.

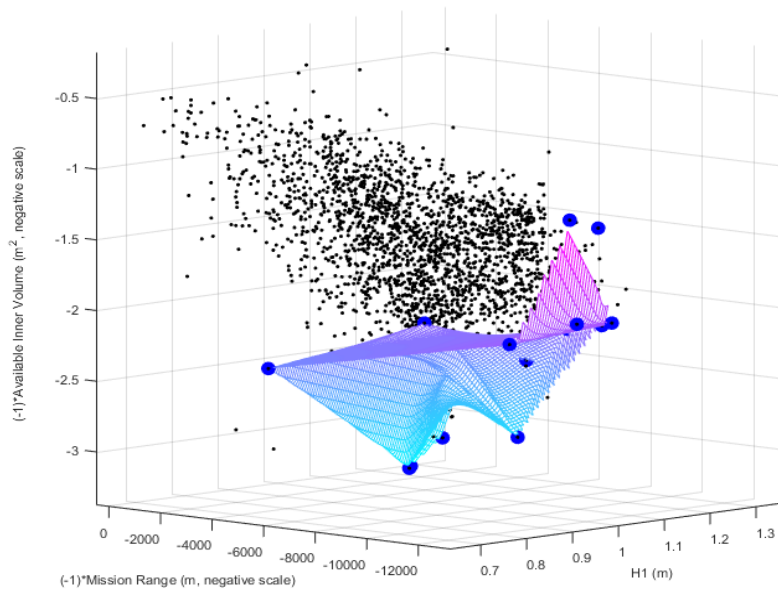


**Figure 32. Three Dimensional Pareto Frontiers via Interpolated Mesh for Optimization**

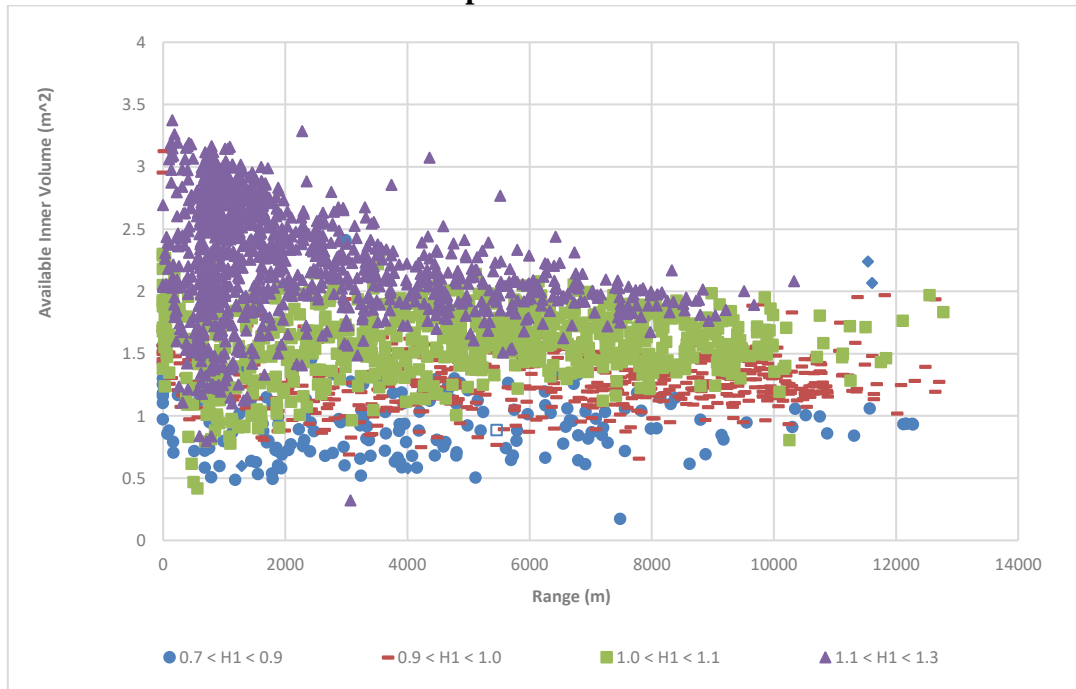


**Figure 33. Three Dimensional Scatter Plot of each Unknown Parameter (H1) for Optimization**

First and most importantly, I have to gather data and proceed optimization. In consequence of sensitivity analysis, parametric range is decided. Constraints and baseline of the model are decided with a reference to Jalbert's paper [17]. Currently it takes five to seven minutes per case. But since three-dimensional modeling, CFD analysis and origami can run at the same time, it can be reduced to 2 to 3 minutes per case with a set of data which is one generation of Genetic Algorithm.

Final goal is to build a high quality model and compare with high quality baseline model where the optimization is started. This high quality model can be also used for 3D printing that I can embark experiment with real model in the future.

## 5. CONCLUSIONS

In this thesis, a design framework for an AUV with origami morphing capabilities was proposed and demonstrated. The present origami design method is applicable to the AUV because its outer shape can be represented as a 2-manifold, orientable surface topologically equivalent to a disk. The novel origami-based design of the AUV proposed here allows the folding and unfolding of the vehicle between the AUV shape optimized for hydrodynamic efficiency (to navigate underwater and store materials) and the planar shape (that maximizes the projected area of the AUV solar panels to charge the power supplies). The AUV designs were evaluated using several software and tools such as ANSYS, Rhinoceros, and in-house codes for origami design. In this particular case, I have focused on optimizing parameters associated with mission range and mobility. Future work will consider other physical characteristics that might be critical to the AUV performance. The folding simulation of the AUV used here only considers kinematics (i.e., the constitutive response of the materials potentially comprising the folds is not considered). Future work will include the consideration of the constitutive response of the active materials (e.g., shape memory alloys or shape memory polymers) that will potentially comprise the folds.

AUV, as an unmanned underwater vehicle, simulated hydrodynamic performance depending on the variables were line with expectations. Minimum drag coefficients ( $C_D$ ) were 0.08 which is the lowest value that the streamlined shape can achieve. In addition, trade-off between available area (*Area*) and available inner volume (*Volume*) is observed clearly. Influence of unknown parameter, *HI*, is also clearly observed.

## REFERENCES

- [1] Zirbel, Shannon A., et al. "An origami-inspired self-deployable array." ASME 2013 Conference on Smart Materials, Adaptive Structures and Intelligent Systems. American Society of Mechanical Engineers, 2013.
- [2] Tachi T. "Geometric considerations for the design of rigid origami structures." In: Proceedings of the International Association for Shell and Spatial Structures (IASS) Symposium. Vol. 12; 2010. p. 458–460.
- [3] Wu W., You Z. "Modelling rigid origami with quaternions and dual quaternions." Proceedings of the Royal Society of London A: Mathematical, Physical and Engineering Sciences. 2010;466(2119):2155–2174.
- [4] Liu S., Chen Y., Lu G. "The rigid origami patterns for flat surface." In: ASME DETC/CIE 2013. American Society of Mechanical Engineers; 2013. p. DETC2013–12947, pp. V06BT07A039.
- [5] Evans T., Lang R., Magleby S., Howell L. "Rigidly foldable origami gadgets and tessellations." Royal Society Open Science. 2015;2(9).
- [6] Zhou X., Wang H., You Z. "Design of three-dimensional origami structures based on a vertex approach." Proceedings of the Royal Society of London A: Mathematical, Physical and Engineering Sciences. 2015;471(2181):20150407.
- [7] Bowers J. "Skeleton structures and origami design." Thesis, University of Massachusetts, Amherst. 2015.
- [8] Tachi T. "Simulation of rigid origami." Origami 4, Fourth International Meeting of Origami Science, Mathematics, and Education. 2009; p. 175–187.
- [9] Filipov E., Paulino G., Tachi T. "Origami tubes with reconfigurable polygonal cross-sections." Proceedings of the Royal Society of London A: Mathematical, Physical and Engineering Sciences. 2016;472(2185):20150607.
- [10] Dudte L. H., Vouga E., Tachi T., Mahadevan L. "Programming curvature using origami tessellations." Nature Materials. 2016;15(5):583–588.
- [11] Dureisseix D. "An overview of mechanisms and patterns with origami." International Journal of Space Structures. 2012;27(1):1–14.
- [12] Gattas J., You Z. "Miura-base rigid origami: parametrizations of curved-crease geometries." Journal of Mechanical Design. 2014;136(12):121404.

- [13] Husaini, M., Samad, Z., Arshad, M. "Autonomous underwater vehicle propeller simulation using computational fluid dynamic", Computational Fluid Dynamics Technologies and Applications, InTech, pp. 293–314, 2011.
- [14] Khairul, A., Ray, T., and Anavatti, S. "Design and construction of an autonomous underwater vehicle." Neurocomputing, 142: 16-29, 2014.
- [15] McCartney, B. S., and P. G. Collar. "Autonomous submersibles-instrument platforms of the future.", 1989.
- [16] Ageev, M. "An analysis of long-range AUV, powered by solar energy." OCEANS'95. MTS/IEEE. Challenges of Our Changing Global Environment. Conference Proceedings. Vol. 2. IEEE, 1995.
- [17] Lutz, T. and Wagner, S. "Numerical shape optimization of natural laminar flow bodies." In: Proceedings of the 21st ICAS congress, Melbourne, Australia, pp.1–11, 1998.
- [18] Bertram V. and Alvarez A., "Hydrodynamic aspects of AUV design", 5th conference on computer and IT applications in the maritime industries (COMPIT), Oegstgeest, Netherlands, pp. 45–53, 2006.
- [19] Alvarez, A, Bertram, V. and Gualdesi, L., "Hull hydrodynamic optimization of autonomous underwater vehicles operating at snorkeling depth" Ocean Eng., 36:105–112, 2009.
- [20] Phillips, A., Turnock, S., and Furlong, M., "The use of computational fluid dynamics to aid cost-effective hydrodynamic design of autonomous underwater vehicles" Proc IMechE Part M: J Engineering for the Maritime Environment, 224: 239–254, 2010.
- [21] Stevenson P., Furlong M. and Dormer D., "AUV shapes combining the practical and hydrodynamic considerations", In: Proceedings of the OCEANS 2007 Europe MTS/IEEE conference and exhibition, Aberdeen, UK, pp.1–6, 2007.
- [22] Joung, T., Sammut, K., He, F. and Lee, S., "A study on the design optimization of an AUV by using computational fluid dynamic analysis" In: Proceedings of the 19th international offshore and polar engineering conference, Osaka, Japan, pp. 696–702, 2009.
- [23] Khairul, A., Ray, T., and Anavatti, S. "A new robust design optimization approach for unmanned underwater vehicle design." Proceedings of the Institution of Mechanical Engineers, Part M: Journal of Engineering for the Maritime Environment, 226.3: 235–249, 2012.

- [24] Samareh, J. "A Survey of Parameterization Techniques", CEAS/AIAA/ICASE/NASA Langley International Forum on Aeroelasticity and Structural Dynamics, Williamsburg, VA, pp. 333–343, 1999.
- [25] Piegl, L., and Tiller, W. *The NURBS Book*, Springer, New York, 1997.
- [26] Piegl, L. "On NURBS: a Survey", *IEEE Computer Graphics and Applications*, Volume 11 Issue 1, Page 55-71, January 1991.
- [27] Hur, D. "Ground vehicle optimization regarding aesthetic completeness and aerodynamic characteristics by modification of vehicle modeling function and conceptual design process", 51st AIAA Aerospace Sciences Meeting including the New Horizons Forum and Aerospace Exposition, Grapevine (Dallas/Ft. Worth Region), Texas, January 2013.
- [28] Peraza Hernandez, E., Hartl, D., Akleman, E., and Lagoudas, D. "Modeling and analysis of origami structures with smooth folds." *Computer-Aided Design*, 78, pp. 93-106, 2016.
- [29] Peraza Hernandez, E., Hartl, D., Lagoudas D. "Design of origami structures with smooth folds." In *ASME 2016 Conference on Smart Materials, Adaptive Structures and Intelligent Systems*, 2016, p. V002T03A018.
- [30] Peraza Hernandez, E., Hartl, D., and Lagoudas, D., "Kinematics of origami structures with smooth folds." *Journal of Mechanisms and Robotics*, 8(6), 2016, p.061019.
- [31] Peraza Hernandez, EA, D. J. Hartl, and D. C. Lagoudas. "Design and simulation of origami structures with smooth folds." In *Proc. R. Soc. A*, vol. 473, p. 20160716. The Royal Society, 2017.
- [32] H.A. Taha, *Operations Research: An Introduction (For VTU)*, 8th edn. Pearson Education India, 1982.
- [33] P.Y. Papalambros, D.J. Wilde, "Principles of optimal design: modeling and computation", Cambridge university press, 2000.
- [34] T.C. Wagner, P.Y. Papalambros, "Selection families of optimal engine designs using nonlinear programming and parametric sensitivity analysis", Tech. rep., SAE Technical Paper, 1997.
- [35] Jalbert, J. "A solar-powered autonomous underwater vehicle." *Oceans 2003. Proceedings*. Vol. 2. IEEE, 2003.

- [36] Blidberg, Ageev, and Jalbert, "Some Design Considerations for a Solar Powered AUV; Energy Management and its Impact on Operational Characteristics", Unmanned Untethered Submersible Technology Sept. 7-10, 1997.
- [37] Calkins, D., and Chan, W. "CD aero - A parametric aerodynamic drag prediction tool", International Congress and Exposition, Detroit, MI, SAE Paper No. 980398, 1998.
- [38] Tovey, M. "Computer-aided vehicle styling," *Comput. Aided Des*, 21(3), pp. 172–179, 1989.
- [39] Lyu, N., and Saitou, K. "Decomposition-based assembly synthesis of space frame structures using joint library," *ASME J. Mech. Des.*, 128, pp. 57–65, 2006.
- [40] Lo, S. "A new mesh generation scheme for arbitrary planar domains", *Int. J. Numer. Methods Eng.*, 21:1403–1426, 1985.
- [41] Zhu, J. Z., Zienkiewicz, O. C., Hinton, E., Wu, J. "A new approach to the development of automatic quadrilateral mesh generation" *Int. J. Numer. Methods Eng.*, 32:849–866, 1991.
- [42] Johnston, B. P., Sullivan, J. M. "A normal offsetting technique for automatic mesh generation in three dimensions" *Int. J. Numer. Methods Eng.*, 36:1717–1734, 1993.
- [43] Jin, H., Tanner, R. I., "Generation of unstructured tetrahedral meshes by advancing front technique", *Int. J. Numer. Methods Eng.*, 36:1805–1823, 1993.
- [44] George, P. L., Seveno, E. "The advancing-front mesh generation method revisited", *Int. J. Numer. Methods Eng.*, 37:3605–3619, 1994.
- [45] Mavriplis, D. "An advancing front Delaunay triangulation algorithm designed for robustness." 31st Aerospace Sciences Meeting. 1992.
- [46] Launder, Brian Edward, and Dudley Brian Spalding. "Lectures in mathematical models of turbulence." 1972.
- [47] Fluent, Ansys. "12.0 Theory Guide.", Ansys Inc 5, 2009.
- [48] Schlichting, Hermann, et al. *Boundary-layer theory*. Vol. 7. New York: McGraw-hill, 1960.
- [49] Wilcox, David C. *Turbulence modeling for CFD*. Vol. 2. La Canada, CA: DCW industries, 1998.

- [50] Bardina, J., et al. "Turbulence modeling validation." 28th Fluid dynamics conference. 1997.
- [51] BYD North America Headquarters, 1800 S. Figueroa Street, Los Angeles, CA90015, USA, Tel: +1-213-748-3980
- [52] EcoDirect, 2834 La Mirada Drive, Suite E Vista, CA 92081
- [53] Tachi, Tomohiro. "Origamizing polyhedral surfaces." IEEE transactions on visualization and computer graphics 16.2 (2010): 298-311.
- [54] Robert McNeel & AssociatesSeattle Weather, Headquarters, North America, and Pacific 3670 Woodland Park Ave N, Seattle, WA 98103 USA.
- [55] Malak, R. J., and Paredis, C. J. J., 2010, "Using Parameterized Pareto Sets to Model Design Concepts," ASME J. Mech. Des., 132(4), p. 041007.
- [56] Lin, J. G., 1976, "Multiple-Objective Problems: Pareto-Optimal Solutions by Method of Proper Equality Constraints," IEEE Trans. Autom. Control, 21(5),pp. 641–650.
- [57] Messac, A., and Mattson, C. A., 2004, "Normal Constraint Method With Guarantee of Even Representation of Complete Pareto Frontier," AIAA J., 42(10), pp. 2101–2111.
- [58] Deb, K., Pratap, A., Agarwal, S., and Meyarivan, T., "A Fast and Elitist Multi-objective Genetic Algorithm: NSGA-II," IEEE Trans. E vol. Comput., 6(2), pp. 182–197, 2002.
- [59] Tax, David MJ, and Robert PW Duin. "Support vector domain description." Pattern recognition letters 20.11 (1999): 1191-1199.
- [60] Hartl, Darren J., et al. "Parameterized design optimization of a magnetohydrodynamic liquid metal active cooling concept." Journal of Mechanical Design 138.3 (2016): 031402.
- [61] Van Beers, Wim CM, and Jack PC Kleijnen. "Kriging interpolation in simulation: a survey." Simulation Conference, 2004. Proceedings of the 2004 Winter. Vol. 1. IEEE, 2004.
- [62] Venkataraman S, and Haftka RT, "Structural optimization complexity: what has Moore's law done for us?", Structural and Multidisciplinary Optimization, Vol. 28, No. 6, pp. 375-387, 2004.

- [63] Sacks J, Welch WJ, Mitchell TJ, and Wynn HP, Design and Analysis of Computer Experiments, *Statistical Science*, Vol. 4 (4), pp. 409-435, 1989.
- [64] Simpson TW, Peplinski JD, Koch PN, and Allen JK, Meta-models for computer based engineering design: Survey and recommendations. *Engineering with Computers*, Vol. 17, No. 2, pp. 129-150, 2001.
- [65] Queipo NV, Haftka RT, Shyy W, Goel T, Vaidyanathan R, and Tucker, PK, Surrogate-based analysis and optimization, *Progress in Aerospace Sciences*, Vol. 41, pp. 1-28, 2005.
- [66] Simpson TW, Toropov V, Balabanov V, and Viana FAC, Design and Analysis of Computer Experiments in Multidisciplinary Design Optimization: a Review of How Far We Have Come – or Not, in: *Proceedings of the 12th AIAA/ISSMO Multidisciplinary Analysis and Optimization Conference*, Victoria, Canada, September 10-12, 2008. AIAA 2008-5802.
- [67] Kleijnen JPC, *Design and analysis of simulation experiments*, Springer Verlag, 2007.
- [68] Forrester AIJ and Keane AJ, Recent advances in surrogate-based optimization, *Progress in Aerospace Sciences*, Vol. 45, No. 1-3, pp. 50-79, 2009.
- [69] Montgomery DC, *Design and analysis of experiments*, John Wiley & Sons, 2004.
- [70] Simpson TW, Lin DKJ, and Chen W, Sampling Strategies for Computer Experiments: Design and Analysis, *International Journal of Reliability and Applications*, Vol. 2, No. 3, pp.209-240, 2001.
- [71] McKay MD, Beckman RJ, and Conover WJ, A Comparison of Three Methods for Selecting Values of Input Variables from a Computer Code, *Technometrics*, Vol. 21, pp. 239-245, 1979.
- [72] Iman RL, and Conover WJ, Small sample sensitivity analysis techniques for computer models, with an application to risk assessment, *Communications in Statistics, Part A. Theory and Methods*, Vol. 17, pp. 1749-1842, 1980.
- [73] Kleijnen JPC, Sanchez SM, Lucas TW, and Cioppa TM, A user's guide to the brave new world of designing simulation experiments, *INFORMS Journal on Computing*, Vol. 17, No. 3, pp. 263-289, 2005.
- [74] Bates, Stuart J., Johann Sienz, and Vassili V. Toropov. "Formulation of the optimal Latin hypercube design of experiments using a permutation genetic algorithm." *AIAA Paper*, 2004-2011, 2004: 1-7.

[75] "Drag of a Sphere." NASA. NASA, 05 May 2015. Web. 05 June 2017.